Carbon stocks and isotopic budgets of the terrestrial biosphere at mid-Holocene and last glacial maximum times

Louis M. François, Yves Goddéris, Pierre Warnant, Gilles Ramstein, Nathalie de Noblet, Stephan Lorenz

Carbon stocks and isotopic budgets of the terrestrial biosphere at mid-Holocene and last glacial maximum times

Louis M. François [a,*], Yves Goddéris [a], Pierre Warnant [a], Gilles Ramstein [b], Nathalie de Noblet [b], Stephan Lorenz [c]

[a] *Laboratoire de Physique Atmosphérique et Planétaire (LPAP), Université de Liège, Avenue de Cointe 5, B-4000 Liège, Belgium*
[b] *Laboratoire des Sciences du Climat et de l'Environnement (LSCE), D.S.M., Orme des Merisiers, Bat. 709, C.E. Saclay, F-91191 Gif-sur-Yvette, France*
[c] *Universität Bremen Fachbereich, Geowissenschaften, Postfach 33 04 40, D-28334 Bremen, Germany*

The carbon fluxes, stocks and isotopic budgets of the land biosphere at mid-Holocene (6 ka BP) and last glacial maximum (21 ka BP) times are reconstructed with the CARbon Assimilation In the Biosphere (CARAIB) model forced with two different sets of climates simulated by the European Centre-HAMburg (ECHAM) and LMD general circulation models. It is found that the trends predicted on the basis of both sets of GCM climatic fields are generally consistent with each other, although substantial discrepancies in the magnitude of the changes may be observed. Actually, these discrepancies in the biospheric results associated with the use of different GCM climatic fields are usually smaller than the differences between biospheric runs performed while considering or neglecting the CO_2 fertilization effect (which might, however, be overestimated by the model due to uncertainties concerning changes in nutrient availability). The calculated changes with respect to the present of the biosphere carbon stock range from -132 to $+92$ Gt C for the mid-Holocene and from -710 to $+70$ Gt C for the last glacial maximum. It is also shown that the relative contribution of the material synthesized by C_4 plants to the total biomass of vegetation, litter and soils was substantially larger at mid-Holocene and last glacial maximum times than today. This change in the relative importance of the C_3 and C_4 photosynthetic pathways induced changes in the ^{13}C fractionation of the land biosphere. These changes in the average biospheric fractionation resulting from the redistribution of C_3 and C_4 plants were partly compensated for by changes of opposite sign in the fractionation of C_3 plants due to the modification of the intercellular CO_2 pressure within their leaves. With respect to present times, the combination of both processes reduced the ^{13}C discrimination i.e., less negative fractionationof the land biosphere by 0.03 to 0.32‰ during the mid-Holocene and by 0.30 to 1.86‰ at the last glacial maximum.

Keywords: Carbon cycle; Biosphere; Pleistocene; Isotopic fractionation; Model

1. Introduction

Ice core measurements (Barnola et al., 1987; Jouzel et al., 1993) have revealed that the CO_2

* Corresponding author. Fax: +32-4-254-7573; e-mail: francois@astro.ulg.ac.be

concentration of the Earth's atmosphere has fluctuated widely over the glacial–interglacial cycles. These CO_2 variations are well correlated with global climatic changes over the same period. Several hypotheses have been put forward to explain these fluctuations in atmospheric CO_2 concentration. Most of these invoke a redistribution of carbon in the ocean–atmosphere system through changes in oceanic circulation and/or the efficiency of the oceanic biological pump (Broecker, 1982; Knox and McElroy, 1984; Sarmiento and Toggweiler, 1984; Siegenthaler and Wenk, 1984; Broecker and Peng, 1989; Martin, 1990). However, more recently, several studies have pointed out that processes such as coral reef buildup and the dissolution of seafloor carbonates (Berger and Keir, 1984; Opdyke and Walker, 1992; Walker and Opdyke, 1995), continental weathering (Gibbs and Kump, 1994; Munhoven and François, 1996) and the sequestration of carbon into the continental biosphere (Adams et al., 1990; Crowley, 1995) may have also influenced the budget of atmospheric CO_2 during Pleistocene and Holocene times. Thus, it is becoming more and more obvious that the ocean–atmosphere system cannot be isolated from the rest of the global carbon cycle to understand the glacial–interglacial CO_2 changes. In particular, the changes over glacial–interglacial times of the land biospheric carbon stocks and fluxes must be reconstructed to provide a full carbon budget for the past system.

Two key periods commonly considered in the study of the changes in the carbon budget of the land biosphere are the last glacial maximum (LGM, 21 ka BP) when the extent of the ice sheets was the largest, and the mid-Holocene (6 ka BP or climatic optimum) prior to which deglaciation was essentially completed. Oceanic and continental data constraining the carbon budget and the land vegetation distribution exist for both time periods. Moreover, climatic reconstructions with general circulation models (GCMs) are also available.

The LGM was a time of low atmospheric CO_2 levels (200 ppmv; Barnola et al., 1987) with a colder and generally drier climate, as well as extensive ice sheets in the northern hemisphere and a sea level 100–120 m lower than at present (CLIMAP Project Members, 1976, 1981; Peltier, 1994). Oceanic carbon isotopic evidence (Duplessy et al., 1988; Bird et al., 1994) and vegetation mapping based on palynological or sedimentological data (Adams et al., 1990; van Campo et al., 1993; Crowley, 1995) both suggest that the continental biosphere (vegetation and soils) currently contains more carbon than at LGM times, indicating that substantial amounts of carbon were transferred from the atmosphere–ocean system to the biosphere during the last deglaciation. Taking into account that the biospheric isotopic composition may have changed, the isotopic method indicates a change of 270–720 Gt C of the biospheric stock from the LGM to the present. The change inferred from the palynological and sedimentological data exhibits a range of 700 to 1350 Gt C. Thus, the palynological and sedimentological data suggest a generally larger change in biospheric carbon stocks than the method based on the carbon isotopic data, although a small overlap exists between the ranges exhibited by both methods. According to Spero et al. (1997), the discrepancy between both types of estimates may even be sharper. Indeed, these authors claim that the shell $\delta^{13}C$ of foraminifera decreases with increasing carbonate ion concentration $[CO_3^{=}]$ of seawater. In their interpretation, a substantial part of the glacial–interglacial $\delta^{13}C$ signal observed in foraminiferal sequences, may be due to $[CO_3^{=}]$ variations and not to global oceanic $\delta^{13}C$ changes. This process may reduce the variation of the land biospheric stock inferred by the isotopic method by more than a factor of 2. Other reconstructions use GCM outputs coupled to bioclimatic schemes and/or biospheric models (Prentice and Fung, 1990; Friedlingstein et al., 1992; Prentice et al., 1993; Esser and Lautenschlager, 1994; Friedlingstein et al., 1995; François et al., 1998) and provide estimates of the change in a range (0–700 Gt C) consistent with values suggested by the isotopic method.

During mid-Holocene times, the climate, ice sheet extent and sea level were similar to the present, and the atmospheric CO_2 concentration recorded in the Vostok ice core was 260–270 ppmv (Barnola et al., 1987). Paleobotanical evidence suggests that the northward limit of boreal forests shifted to higher latitudes (Ritchie et al., 1983) and that grasslands and savannas covered a large fraction of the modern Sahara desert (Street-Perrott and Perrott, 1993). Climatic simulations for that period indicate a strengthening of the summer African monsoon which pro-

vided more moisture in the Sahelian and southern Sahara regions (Mitchell et al., 1988) which may have stimulated vegetation growth in currently desertic areas. This strengthening of the African monsoon results directly from the changes in the Earth's orbital parameters which increase the amplitude of the seasonal cycle of solar radiation and, hence, the temperature contrast between land and sea. However, these climatic simulations appear to underestimate the magnitude of the monsoon enhancement. Kutzbach et al. (1996) showed that stronger monsoons, implying larger vegetation shifts, can be obtained if vegetation and soil changes are taken into account in such climatic simulations. Such results emphasize the important role played by vegetation feedbacks in regulating climate changes (de Noblet et al., 1996; Gallimore and Kutzbach, 1996). The biospheric carbon fluxes and stocks for the mid-Holocene have been reconstructed by Foley (1994) using the DEMETER biospheric model forced with the climatic fields from the GENESIS GCM and the vegetation distribution calculated with the BIOME model (Prentice et al., 1992). According to this reconstruction, the biospheric carbon stock was larger by 35 Gt C at mid-Holocene times with respect to the present.

In this paper, we present a new reconstruction of the land biosphere carbon budget at mid-Holocene and LGM times. For this purpose, we use the CARbon Assimilation In the Biosphere model (CARAIB, Warnant et al., 1994) forced by climates simulated by two different GCMs. The use of the same tools for both periods provides a better comparison of the model estimates of carbon stock and flux changes at mid-Holocene and LGM times. Moreover, the methodology also allows an estimation of the uncertainties associated with the use of different GCM climatic fields. We also test the importance of CO_2 fertilization, although a more detailed study would incorporate the effects of changes in nutrient availability. Finally, we analyse changes in the distribution of C_3 and C_4 plants and in the ^{13}C discrimination of land vegetation.

2. The input climatic fields

The climatic fields used to force the CARAIB biosphere model are from two different atmospheric general circulation models participating in the Paleo-Modelling Intercomparison Project (PMIP; Joussaume and Taylor, 1995): European Centre-HAMburg (ECHAM) version 3.6 and LMD version 5.3. In the following text, we will refer to the first of these models as ECHAM and to the second as LMD-LSCE. Both of these models were run for present-day (control run), mid-Holocene (6 ka) and LGM (21 ka) conditions. The values of the obital parameters used for these periods are listed in Table 1. The models are briefly described below.

2.1. The ECHAM model

The ECHAM-3 model is the third generation of the general circulation model developed at the Max-Planck-Institut für Meteorologie, Hamburg, Germany and at the University of Hamburg. As the previous ECHAM versions and as the European Centre for Medium Range Weather Forecasts (ECMWF, Reading, United Kingdom) model, from which the ECHAM evolved, ECHAM-3 is based on the primitive equations. Details about its formulation are contained in the model documentation (DKRZ, 1994) and in the work of Roeckner et al. (1992), which also contains basic diagnostic information on the model's climatology. Only a brief description of the model is given here.

Prognostic variables are vorticity, divergence, temperature, water vapour, cloud water and surface

Table 1
Orbital parameters used in the various model simulations. The longitude of perihelion is taken from northern hemisphere spring equinox

	Present (0 ka)	Mid-Holocene (6 ka)	LGM (21 ka)
Eccentricity	0.016724	0.018682	0.018994
Obliquity (°)	23.447	24.105	22.949
Longitude of perihelion (°)	282.16	180.92	294.42

pressure. Except for the water components, the prognostic variables are represented by spherical harmonics with triangular truncation at a distinct wave number. For the PMIP experiments, the high resolution model was used with truncation at wave number 42 (T42). Nonlinear terms and physical processes are evaluated at grid points of a corresponding Gaussian grid providing a nominal resolution in latitude and longitude of 2.8125° in the case of the T42 model. The vertical representation is realised in a hybrid sigma-pressure system by 19 irregularly spaced vertical levels up to a pressure level of 10 hPa. The integration is performed following a semiimplicit scheme with a leap-frog time filter. The time step is 24 min for dynamics and physics, except for radiation which is calculated at 2 h intervals.

The radiation scheme is based on a two-stream approximation of the radiative transfer equations with six spectral intervals in the infrared and four in the solar spectrum (Hense et al., 1982). Scattering and absorption due to water vapour, clouds, carbon dioxide, ozone and aerosols are taken into account; in the terrestrial portion scattering is neglected. The land surface scheme (Dümenil and Todini, 1992) considers the heat and water budgets of snow cover, vegetation, and in the soil, where the heat transfer is solved in a five-layer model with zero heat flux at the lowest soil layer. Besides the separation of the land surface into land ice, snow covered and bare land, there exist no land characteristics. The surface background albedo over land is taken from satellite data (Geleyn and Preuss, 1983) and the actual albedo of snow covered land is calculated with respect to surface temperature and prescribed ratios of vegetation and forest.

The ECHAM-3 (T42) model is able to simulate most aspects of the presently observed time-mean circulation and its variations with remarkable skill (Roeckner et al., 1992). There are still a few problem areas, but the errors are much less pronounced than in simulations with earlier model versions.

The two paleoclimate experiments with the ECHAM model within PMIP have been run with a fixed climatological cycle of sea surface temperatures (SSTs). The annual cycle for the control run and for the mid-Holocene simulation consists of 12 monthly means which are the average of the period 1979–1988 of the AMIP (Gates, 1992) dataset. The annual cycle of SST (including the distribution of sea ice) for the LGM was approximated by a sine function, taking the reconstruction of the minimum and maximum SSTs of the CLIMAP datasets (CLIMAP Project Members, 1981) as values for February and August. SSTs during model integrations are updated every time step by linear interpolation of monthly mean data, attributed to the central days of successive months.

For the true representation of insolation at the top of the atmosphere, the calculation of the solar zenith angle in the ECHAM model has been adapted with respect to the orbital parameters for all three experiments (Table 1). The equivalent CO_2 concentrations were set to 200 ppm for the LGM, 280 ppm for the mid-Holocene and 345 ppm for the control run. The adjustment of the remaining boundary conditions for the last glacial maximum (distribution of land/sea and terrain heights due to the sea level drop of 105 m; ice sheets due to a new reconstruction of Tushingham and Peltier (1991); surface background albedo, vegetation and forest ratio at modern values unless suppressed by overlying glacial ice sheets) have been performed according to the definitions given by PMIP.

2.2. The LMD-LSCE model

The LMD-LSCE climatic experiments used in this paper have been performed with the LMD AGCM version 5.3. This is a grid point model using an Arakawa C-grid (see Sadourny and Laval, 1984 for a more exhaustive description). The radiation scheme is the same as used in the ECMWF model: the solar portion is a refined version of the scheme developed by Fouquart and Bonnel (1980) and the terrestrial component is from Morcrette (1991). The boundary layer is parameterized using a diffusive equation were the mixing coefficients depend on a prescribed length scale and a diagnostic determination of the turbulent kinetic energy. Condensation is parameterized separately for convective and nonconvective clouds. Convection is parameterized using in sequence a moist adiabatic adjustment and a modified version of the Kuo (1965) algorithm. A prognostic equation for cloud water is included in the model: sources and sinks of cloud condensed water are

parameterized, and the large scale transport is taken into account.

The main new features of the LMD5.3 version are the treatment of the surface and the surface–atmosphere interaction. This version includes a subgrid representation of fractional sea ice cover. A distribution between 8 biomes represents, for each cell, the type of vegetation. The surface scheme representing the hydrologic exchanges between the atmosphere and the biosphere is SECHIBA (Ducoudré and Laval, 1993). The albedo is computed from the snow depth, cover and age, and vegetation cover (Chalita and le Treut, 1994). For all the simulations, we have used the standard resolution, corresponding to 64 points regularly spaced in longitude, 50 points regularly spaced in the sine of latitude, and 11 vertical levels of normalized pressure coordinates. Each experiment includes the full seasonal cycle and lasts 16 years. Averages are made over the last 15 years.

The simulations of the present (control), the mid-Holocene (6 ka) and the LGM (21 ka) climates are fixed SST experiments. As prescribed in PMIP (Joussaume and Taylor, 1995; Ramstein et al., 1998), for 6 ka, the only changes taken into account are the insolation at the top of the atmosphere and the atmospheric CO_2 decrease from 345 ppm (control) to 280 ppm. For 21 ka, the CO_2 is set at 200 ppm (Barnola et al., 1987), the change in insolation is weak, the SST field is deduced from the CLIMAP Project Members (1981) and the ice sheet reconstruction from Peltier (1994).

2.3. Treatment of the GCM climatic fields

The treatment applied to the GCM climatic fields before their use as inputs to the biospheric model is as described by François et al. (1998). Since simulations of present-day climate with GCMs usually show substantial deviations from the observation, only the anomalies of the GCMs are used to reconstruct past climates. The anomaly Δq of a climatic variable q is defined here as a weighted mean between an absolute anomaly Δq_{abs} and a relative anomaly Δq_{rel}:

$$\Delta q = \xi \Delta q_{\mathrm{abs}} + (1 - \xi)\Delta q_{\mathrm{rel}}, \tag{1}$$

with:

$$\Delta q_{\mathrm{abs}} = q_{\mathrm{past}} - q_{\mathrm{pres}}, \tag{2a}$$

$$\Delta q_{\mathrm{rel}} = \frac{q_{\mathrm{obs}}}{q_{\mathrm{pres}}}(q_{\mathrm{past}} - q_{\mathrm{pres}}), \tag{2b}$$

where q_{past} and q_{pres} are respectively the past (LGM or mid-Holocene) and the present-day (control) values of the climatic variable q in the GCM simulations, while q_{obs} is its present-day value in an observation data file. The corrected value q_{cor} of the variable q used to force the biospheric model is then obtained as:

$$q_{\mathrm{cor}} = q_{\mathrm{obs}} + \Delta q. \tag{3}$$

The weighting factor ξ is defined in such a way that it converges towards 1 when the value of q_{cor} derived from the absolute correction (i.e., $q_{\mathrm{obs}} + \Delta q_{\mathrm{abs}}$) is significantly larger than a prescribed positive threshold and that it converges towards 0 when the same value of q_{cor} tends towards 0 or is negative. This procedure offers the possibility of avoiding the presence of negative values of q_{cor} in the corrected dataset when negative values are physically meaningless. Moreover, adopting a relatively small value for the threshold allows the possibility of preferentially selecting the absolute correction. Indeed, in this case, the weighting factor ξ is generally equal to 1, except for a few grid cells where an absolute correction would tend to yield negative values.

This treatment is applied to the GCM air temperature (T), precipitation (P) and cloud cover (C) data. The observational datasets (T_{obs}, P_{obs} and C_{obs}) are from Cramer and Leemans (personal communication, 1995), an updated version of the climatology of Leemans and Cramer, 1991. The original data at $0.5° \times 0.5°$ latitude–longitude resolution have been averaged on the $1° \times 1°$ continental grid of CARAIB. The GCM results (q_{pres} and q_{past}) are interpolated from the original GCM resolution to the same $1° \times 1°$ grid and Eqs. (1), (2a), (2b) and (3) are then used to calculate the corrected climatic fields (q_{cor}). In the case of air temperature (in °C), the value of ξ is always taken equal to 1, corresponding to a purely absolute correction.

This procedure is used to correct both the mid-Holocene (6 ka) and the LGM (21 ka) datasets. For 6

ka, the continental grid is the same as at present and neglects any variation of the continental area due to sea level or isostatic changes. For 21 ka, however, the continental grid is defined by selecting the $1^\circ \times 1^\circ$ grid cells with an elevation higher than -100 m in the topographic database from the Scripps Institution of Oceanography (Gates and Nelson, 1975). Due to this sea level lowering, the continental area at the LGM is increased by 16.7×10^6 km^2 (Antarctica not included) with respect to the present. As required by the correction scheme, the observed fields (T_{obs}, P_{obs} and C_{obs}) have been extrapolated to the LGM land grid points which are currently below sea level by using a distance weighted averaging procedure. The cloud cover fields are used in the biospheric model to estimate the solar radiation fluxes incident at the Earth's surface. In this calculation, the values for the orbital parameters are the same as those used in the general circulation models. However, the surface solar flux is related to the top-of-atmosphere flux through the empirical Ångström relationship (Landsberg, 1986).

The GCM fields of surface horizontal wind speed W_h used by CARAIB in the evaluation of the vertical transfers of CO_2 and water (aerodynamic resistance formalism) are interpolated to the $1^\circ \times 1^\circ$ grid of the biospheric model without making use of the above correction scheme. Two biospheric control runs are hence necessary to describe the present-day states of the biosphere corresponding to the wind fields of both GCMs. Relative air humidity 'RH' is also used by CARAIB to evaluate the stomatal resistance, but this data was not provided by the PMIP dataset. As a result, relative air humidity is not changed from LGM or mid-Holocene to the present and is set to the standard field (i.e., monthly average ECMWF air humidity fields for 1991) used in CARAIB simulations.

3. The biosphere model

3.1. Vegetation distribution

Maps of potential vegetation are derived for each climatic configuration from the bioclimatic scheme of Friedlingstein et al. (1992). This scheme predicts the occurrence of the following vegetation types as a function of temperature and precipitation: permanent ice, desert, tundra, coniferous forest, deciduous forest, grassland, savanna, evergreen rainforest and tropical seasonal forest. Several vegetation types may coexist within a single grid cell: if the climatic conditions are favorable to the presence of n different vegetation types, the fractional cover of each of them is assumed to be $1/n$. These vegetation types are then converted according to the classification used in CARAIB into grasses, needleleaf forest, evergreen broadleaf forest, deciduous broadleaf forest and areas devoid of vegetation. Permanent ice is assumed to be completely devoid of vegetation. Deserts are a priori covered by 90% grasses and 10% broadleaf deciduous trees. Tundras are assumed to be composed of 90% grasses and 10% needleleaf trees. Coniferous forests correspond to 90% coverage of needleleaf trees and 10% of grasses, deciduous forests to 90% broadleaf deciduous trees and 10% grasses, grasslands to 90% grasses and 10% broadleaf deciduous trees, savannas to 67% grasses and 33% broadleaf deciduous trees. Evergreen rainforests are assumed to be covered by 90% evergreen broadleaf trees and 10% grasses. To be consistent with the present-day distribution of tropical evergreen forests in the standard vegetation dataset of CARAIB, the tropical seasonal forest biome of the bioclimatic scheme is assumed to correspond to rainforests and, hence, is also composed of 90% evergreen broadleaf trees and 10% grasses.

The distribution of desertic areas and the fraction of C_3 and C_4 grasses are a posteriori estimated from the net primary productivity (NPP) calculated by CARAIB. Areas free of permanent ice with NPP $= 0$ are considered as extreme deserts. Similarly nonice areas with $0 < 180$ g C m^{-2} year^{-1} are referred to as semideserts. The grasses present in the grassland or the semidesert vegetation classes are subdivided into C_3 and C_4 types as a function of the calculated productivity ratio:

$$r = \frac{\mathrm{NPP_{C4}}}{\mathrm{NPP_{C3}} + \mathrm{NPP_{C4}}}, \qquad (4)$$

where $\mathrm{NPP_{C3}}$ and $\mathrm{NPP_{C4}}$ are the net primary productivities of C_3 and C_4 species, respectively. The

fraction f_{c4} of C_4 vegetation within the grasses is given by:

$$f_{c4} = \begin{cases} 0 \\ a + br \\ 1 \end{cases} \quad \text{if} \begin{cases} r \le -a/b \\ -a/b < r < (1-a)/b \\ r \ge (1-a)/b \end{cases} \tag{5}$$

where the coefficients $a = -0.406$ and $b = 1.46$ have been determined by least square fit (François et al., 1998), so as to best approximate the C_4 distribution in North American grasslands reported by Teeri and Stowe (1976).

With these relationships, the fractions of C_3 and C_4 grasses depend on their respective productivities which means that, besides climate, they also respond to atmospheric CO_2 changes through the fertilization effect. The same is true of desertic areas, since their extent is also determined from productivity criteria. Consequently, deserts can grow when atmospheric CO_2 is reduced. In the simple scheme used here, however, the vegetation cover at a given site is not affected by CO_2 fertilization except for the C_3/C_4 fraction in grasses. In other words, the site may become less productive and eventually fall in the desert category, but forested areas, for instance, cannot be replaced by grasslands in response to CO_2 changes alone. This is a serious limitation of the current version of our model which may substantially affect the distribution of vegetation types during glacial times. These topics should be addressed in future studies.

3.2. Carbon fluxes and stocks

The carbon fluxes and stocks are calculated with the CARbon Assimilation In the Biosphere (CARAIB) model (Warnant et al., 1994; Nemry et al., 1996; Hubert et al., 1998). This model involves various modules associated with the water budget, the leaf level processes, the integration over the canopy, the rate of wood respiration and the amount of soil organic carbon.

The water budget module Improved Bucket Model (IBM) uses a one-day timestep. The monthly climatic data are transformed into daily data by using the stochastic weather generator (with renormalization to the monthly mean) developed by Hubert et al. (1998). In the budget, snowfall, rainfall, snowmelt, evapotranspiration, drainage and surface runoff are considered. The calculation for evapotranspiration is based on Penman's equation.

Photosynthesis at the leaf level is calculated from schemes for C_3 and C_4 species of Farquhar et al. (1980) and Collatz et al. (1992), respectively. The stomatal regulation is described using the formulation of Ball et al. (1987). A typical diurnal variation in the photosynthetic rate is calculated once a month and integrated over the canopy. Wood biomass is assumed to be constant over the year and is related to the fraction of carbon assimilation allocated to wood growth.

The annual mean soil heterotrophic respiration is forced to be equal to the annual mean NPP, assuming that the vegetation–soil system is in equilibrium. The total amount of carbon in litter and soil is derived from this assumption, by using temperature-dependent and soil water-dependent characteristic times for heterotrophic respiration. The assumed temperature dependence is exponential (Q_{10} function) and has been calibrated separately for forests and grasslands using data from Raich and Schlesinger (1992). The soil water dependence is taken from Raich et al. (1991): as soil water is increased, the heterotrophic respiration rate initially increases until an optimum soil water is reached beyond which the rate begins to decrease. The various parameters used in this formulation (e.g., optimum soil water) depend on the soil textural class. More details on the way soil carbon is handled in this version of CARAIB can be found in the work of Nemry et al. (1996).

3.3. ^{13}C isotopic fractionation

The ^{13}C fractionation Δ of photosynthesis with respect to atmospheric CO_2 is evaluated every 2 h in each canopy layer from the following equations (O'Leary, 1993; Hunt et al., 1996):

$$\Delta(‰) = -4.4 - 22.6\frac{c_i}{c_a} \qquad \text{for } C_3 \text{ plants,} \tag{6a}$$

$$\Delta(‰) = -4.4 + 1.4\frac{c_i}{c_a} \qquad \text{for } C_4 \text{ plants,} \tag{6b}$$

where c_i is the intercellular CO_2 pressure within the leaf and c_a is the atmospheric CO_2 pressure. The value of c_i is estimated in the leaf level module of CARAIB. It is assumed that no net isotopic fractionation of ^{13}C occurs during respiration processes.

In this paper, we will present yearly average values for the ^{13}C fractionation of the major vegetation types of the world. The averages over canopy layers and over time are gross primary productivity weighted means, since ^{13}C discrimination occurs during photosynthesis. By contrast, spatial averages over a series of model grid cells are performed as biomass weighted means. A more complete model could calculate the changes over the year of the isotopic composition of all major plant and soil carbon reservoirs. However, the use of the simple average of the fractionation calculated here is adequate for calculating the annual mean value for the biospheric isotopic composition, since the vegetation–soil system is assumed to be in equilibrium at an annual timescale.

4. Results

Several CARAIB simulations were performed with the different GCM climates used in this study at various atmospheric CO_2 levels. The first two simulations are the control runs for modern climate (Cramer and Leemans' climatology with wind speed from the GCM control runs) and preindustrial atmospheric CO_2 (280 ppmv). Global values for air temperature, precipitation and the major biospheric results in these control simulations are listed in Table 2. The small differences between the global values of the biospheric variables associated with the two GCMs are only due to differences in wind speed. For mid-Holocene (6 ka) and LGM (21 ka) times, two biospheric simulations are performed per GCM run: one with the preindustrial atmospheric CO_2 amount (*high* CO_2—no change in CO_2 fertilization, 280 ppmv) and the second with a reduced CO_2 level (reduced CO_2 fertilization, 260 ppmv at 6 ka and 200 ppmv at 21 ka). The results of these various simulations are analysed in this section, after a short description of the climate changes at 6 and 21 ka with respect to the present in both GCM reconstructions.

4.1. Climate distribution

The air temperature and precipitation anomalies with respect to the present (i.e., Δq in Eq. (3)) calculated for 6 and 21 ka in the ECHAM and LMD-LSCE models are shown in Figs. 1–4 on the $1° \times 1°$ continental grids corresponding to both time periods. These anomalies have been averaged over two different seasons: northern hemisphere winter (December–January–February) and summer (June–July–August). Both models provide generally consistent trends at large spatial scales, although substan-

Table 2
Present-day global values of the major climatic and biospheric variables in the control CARAIB simulations

	Acceptable values	ECHAM	LMD-LSCE
Continental area (10^6 km^2)		134.2	134.2
Air temperature (°C)		12.87	12.87
Precipitation volume (km^3 year^{-1})		106,416	106,416
NPP (Gt C year^{-1})	45–62	57.3	56.4
Living phytomass (Gt C)	420–660	646	650
Soil carbon (Gt C)	1200–1800	1379	1334
Total carbon (Gt C)	1820–2460	2025	1984
Fraction of C_4 biomass in total carbon		0.212	0.195
^{13}C fractionation (‰)		−16.39	−16.55
$\delta^{13}C$ of preindustrial biosphere (‰)		−22.89	−23.05

Both simulations differ only by fields of surface horizontal wind speed which are taken from ECHAM or LMD-LSCE model runs. Air temperature and precipitation data are from Cramer and Leemans (personal communication, 1995). Continental area does not include Antarctica. For comparison, a range of acceptable values (Tinker and Ineson, 1990) is given for NPP and carbon stocks.

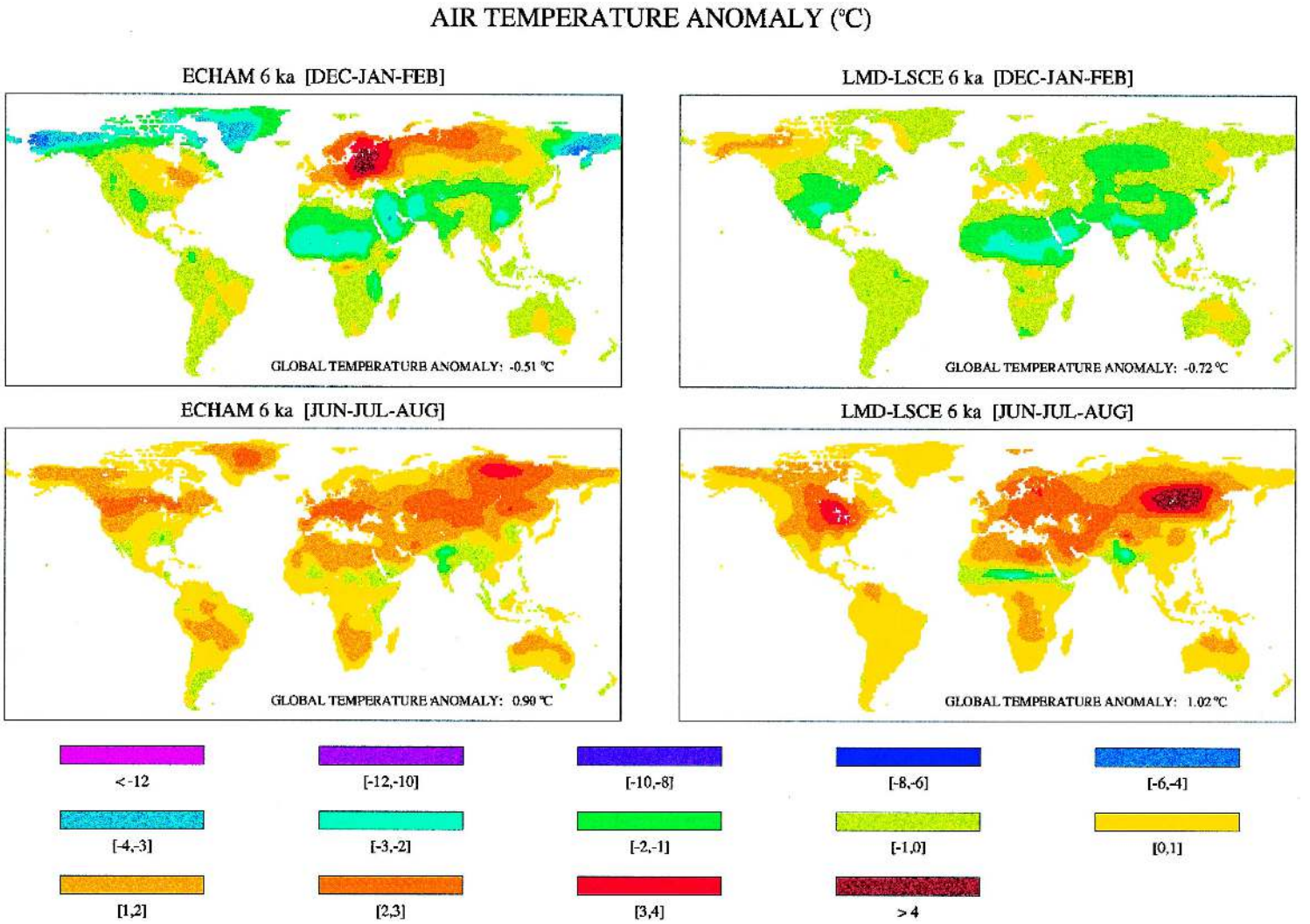

Fig. 1. Geographical distribution of air temperature anomalies (°C) calculated with respect to the present from Eq. (3) for the mid-Holocene (6 ka) using results from ECHAM and LMD-LSCE model simulations. The anomalies have been averaged over the northern hemisphere winter (December–January–February) and summer (June–July–August) periods.

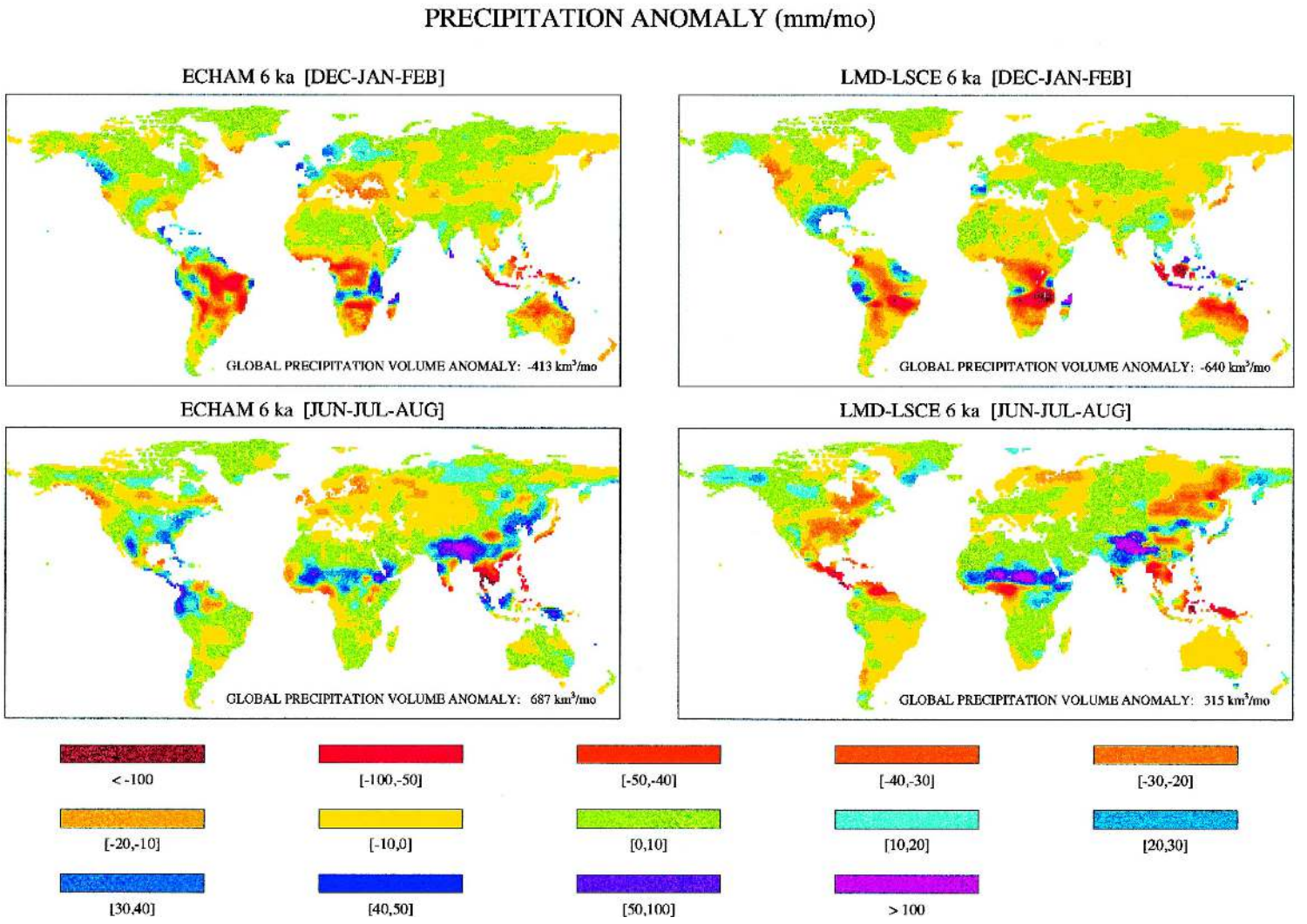

Fig. 2. Geographical distribution of precipitation anomalies (mm month^{-1}) calculated with respect to the present from Eq. (3) for the mid-Holocene (6 ka) using results from ECHAM and LMD-LSCE model simulations. The anomalies have been averaged over the northern hemisphere winter (December–January–February) and summer (June–July–August) periods.

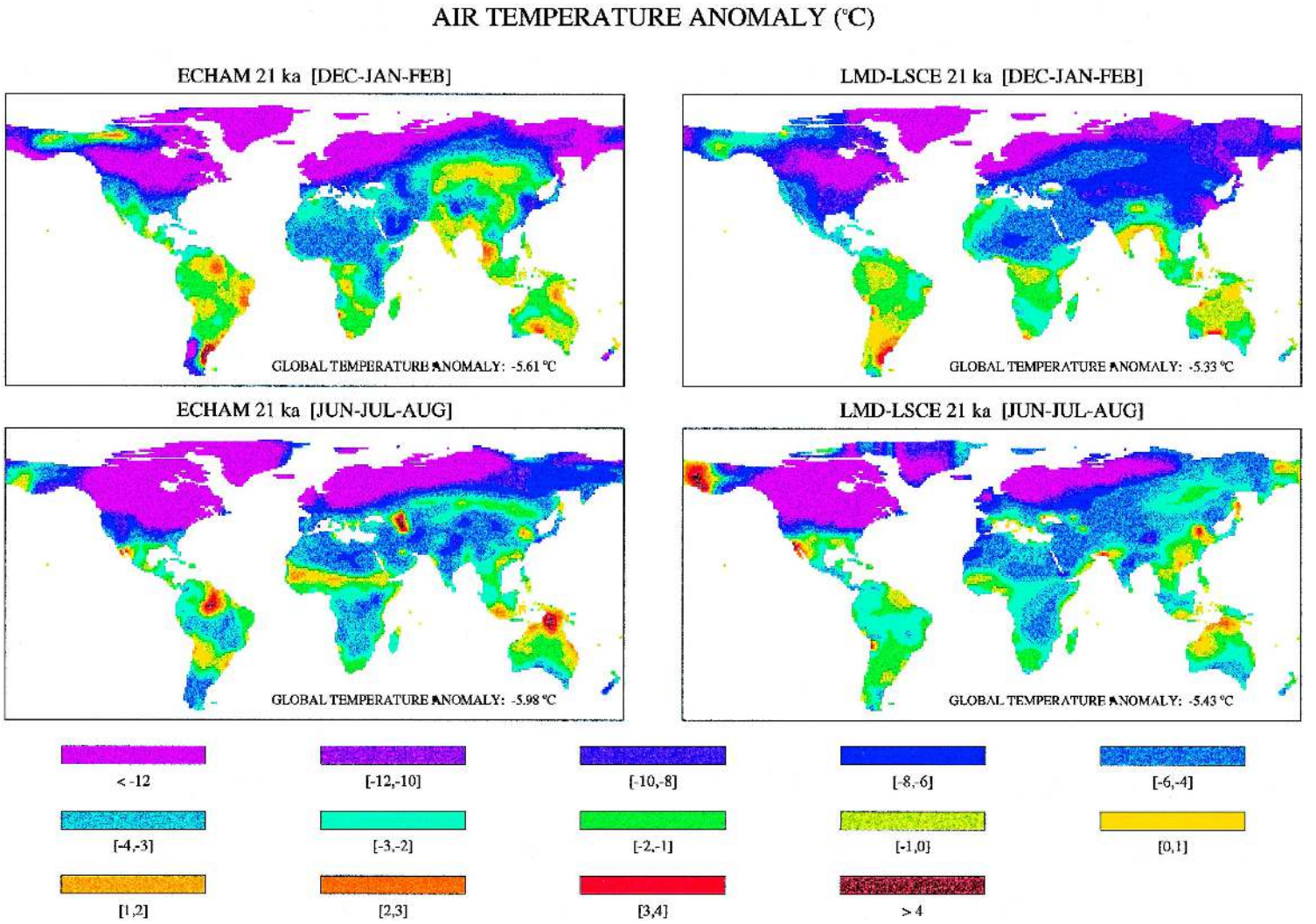

Fig. 3. Geographical distribution of air temperature anomalies (°C) calculated with respect to the present from Eq. (3) for the LGM (21 ka) using results from ECHAM and LMD-LSCE model simulations. The anomalies have been averaged over the northern hemisphere winter (December–January–February) and summer (June–July–August) periods.

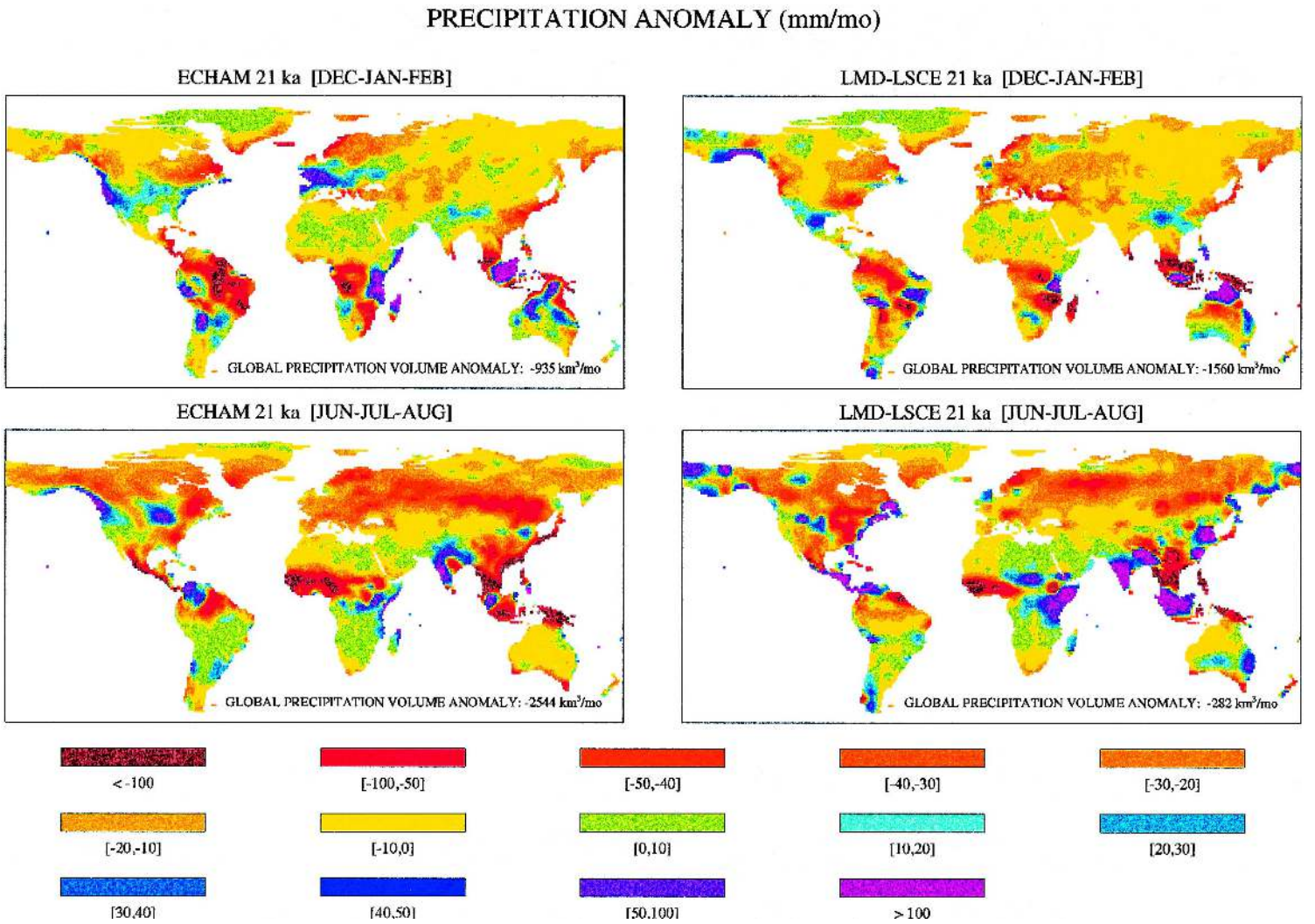

Fig. 4. Geographical distribution of precipitation anomalies (mm year^{-1}) calculated with respect to the present from Eq. (3) for the LGM (21 ka) using results from ECHAM and LMD-LSCE model simulations. The anomalies have been averaged over the northern hemisphere winter (December–January–February) and summer (June–July–August) periods.

tial differences occur at a more regional level. This overall consistency between the two datasets largely results from the fact that all climatic experiments were performed with prescribed SST fields (common to both models).

At 6 ka, the overall temperature trend is a cooling during the northern hemisphere winter and a warming during summer with respect to the present. As a result, the seasonal amplitude of the global land temperature signal increases by 1.41°C for ECHAM and 1.74°C for LMD-LSCE simulations. Regionally, the trends may be reverted with respect to these global trends. For instance, during northern hemisphere winter, the ECHAM model predicts a rather important warming over Europe, Siberia and the eastern part of North America. However, such a warming is not consistent with LMD-LSCE results, which generally show a cooling over the same regions. During northern hemisphere summer, both model reconstructions show a strong warming over Europe and northern Asia, while a cooling is predicted in southern Sahara. This latter cooling should tend to reduce evapotranspiration. Combined with the summer precipitation increase in the region (also predicted by both GCMs), this evapotranspiration change should result in a northward shift of vegetation in southern Sahara at the expense of the desert. These climatic changes are associated with an intensification of the African summer monsoon driven by the enhanced land–ocean contrast resulting from the change in orbital parameters (Kutzbach et al., 1996). Similarly, a cooler and wetter climate during summer months is also predicted over northern India and the Himalayan region, again for both GCMs. Another common feature is a decrease of precipitation (mainly during northern hemisphere summer) over the tropical regions currently covered by rainforests. Some differences in the trends predited by both GCMs exist, however, such as over the eastern part of the United States where ECHAM results suggest a marked increase in precipitation during summer contrasting with a large reduction for the LMD-LSCE model. Globally, the combination of these changes translates into virtually no variation of the annual mean land temperature for both GCM climatic fields, and into an increase by 1867 $km^3\ year^{-1}$ of ECHAM precipitation and a small decrease of 305 $km^3\ year^{-1}$ with the LMD-LSCE model.

At 21 ka, the continents are generally thought to have been much colder and generally drier than today. Both GCMs tend to reproduce these general features of LGM climate. The cooling varies from 2 to 3°C near the equator to more than 12°C in boreal regions (where ice caps were present). Despite this global tendency towards cooling, some areas of the continents exhibit a slight warming, as in northern Australia, Malaysia–Indonesia and South America. The most striking difference between both GCMs is the warming in central Asia, predicted during winter by the ECHAM model and contrasting with the 6–10°C cooling in the same region shown in LMD-LSCE results for the same period and the same region. Although both GCMs predict an overall drying of the continents, many details of the precipitation trends differ markedly among the two models. For instance, during northern hemisphere summer, Central America tends to be drier in ECHAM while it is wetter in LMD-LSCE results. The same discrepancy is also observed during the same period on the eastern coast of the United States and Canada, as well as over eastern China. With respect to the present, the global annual mean temperature over land decreases by 6.25°C in the ECHAM simulation and by 5.55°C for LMD-LMCE. Regarding global precipitation over land, ECHAM predicts a decrease by 1476 $km^3\ year^{-1}$ and LMD-LSCE an increase by 4548 $km^3\ year^{-1}$.

4.2. Vegetation distribution

Fig. 5 shows the changes with respect to the present of the areal coverage of the CARAIB potential vegetation types in all of the simulations performed for mid-Holocene (6 ka) and LGM (21 ka) times. For each time period, simulations with high and reduced CO_2 levels are performed for both sets of GCM climates. The vegetation classification is that of CARAIB, including desertic areas predicted on the basis of productivity criteria, as described in Section 3.1. The responses of both GCMs to the climatic changes appear to be relatively consistent. It should be remembered that in the procedure used in the classification, CO_2 fertilization does not affect the forested areas, except when their productivity becomes so low that they are considered to be deserts. For this reason, the areas of forests at 6 and

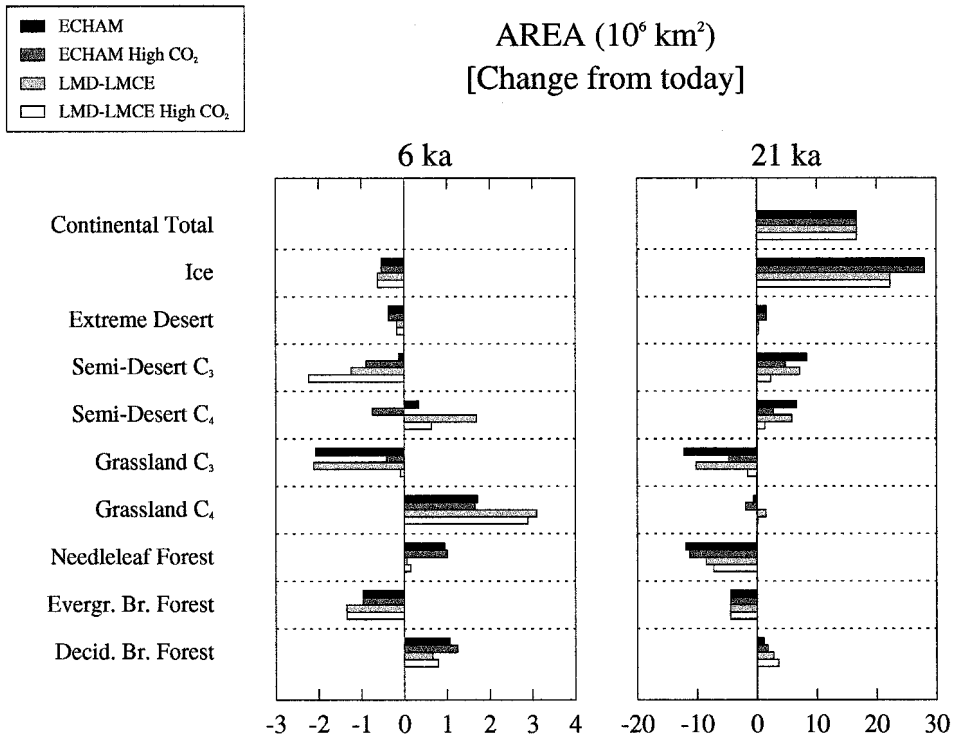

Fig. 5. Changes with respect to the present of the biome areas at the mid-Holocene (6 ka) and the LGM (21 ka) calculated by using ECHAM and LMD-LSCE «corrected» climates. The results obtained both by considering (*ECHAM* and *LMD-LSCE* runs) or neglecting (*ECHAM High* CO_2 and *LMD-LSCE High* CO_2 runs) CO_2 fertilization are illustrated. Note the difference in the scale of the abscissa for 6 and 21 ka.

21 ka are probably overestimated in the reconstruction.

In mid-Holocene times, it is assumed that the total land area is not changed with respect to the present. An expansion of C_4 ecosystems, needleleaf and deciduous broadleaf forests is predicted by all of the simulations, at the expense of permanent ice, C_3 semideserts or grasslands, and evergreen broadleaf forests. The expansion of C_4 ecosystems by 2×10^6–3×10^6 km^2 is largely due to changes in the climatic conditions which become more favorable for their development. The effect of the decrease in the atmospheric CO_2 level from 280 to 260 ppmv (reduction in CO_2 fertilization) is small by comparison except in semideserts. The direction of the CO_2-driven shift is nevertheless towards an increase of the areas of C_4 grasslands which tend to replace less productive C_3 grasses. In contrast, the response of C_3 grasses to the CO_2 change is larger than the climate-driven change. The overall changes obtained here for 6 ka are in overall agreement with those derived by Foley (1994), although the comparison is not always obvious due to the use of a different biome classification. Indeed, in this reconstruction, the areas of cool grasslands and tundras appear to be smaller at 6 ka, consistent with our reduction of C_3 grasslands. Moreover, the area of warm (C_4) grasses also tend to expand. The area of all types of deserts is reduced, consistent with the trend obtained here for extreme deserts and C_3 semideserts. The changes in forests ecosystems also appear consistent, suggesting a slight reduction in evergreen tropical forests and an increase in the area of taiga and coniferous forests as well as cold and temperate deciduous forests.

The areal changes in vegetation types at the LGM are much larger than for the mid-Holocene, since the climatic and CO_2 variations (280 to 200 ppmv) involved are much more important and the present-day shelf (16.7×10^6 km^2) was covered by vegeta-

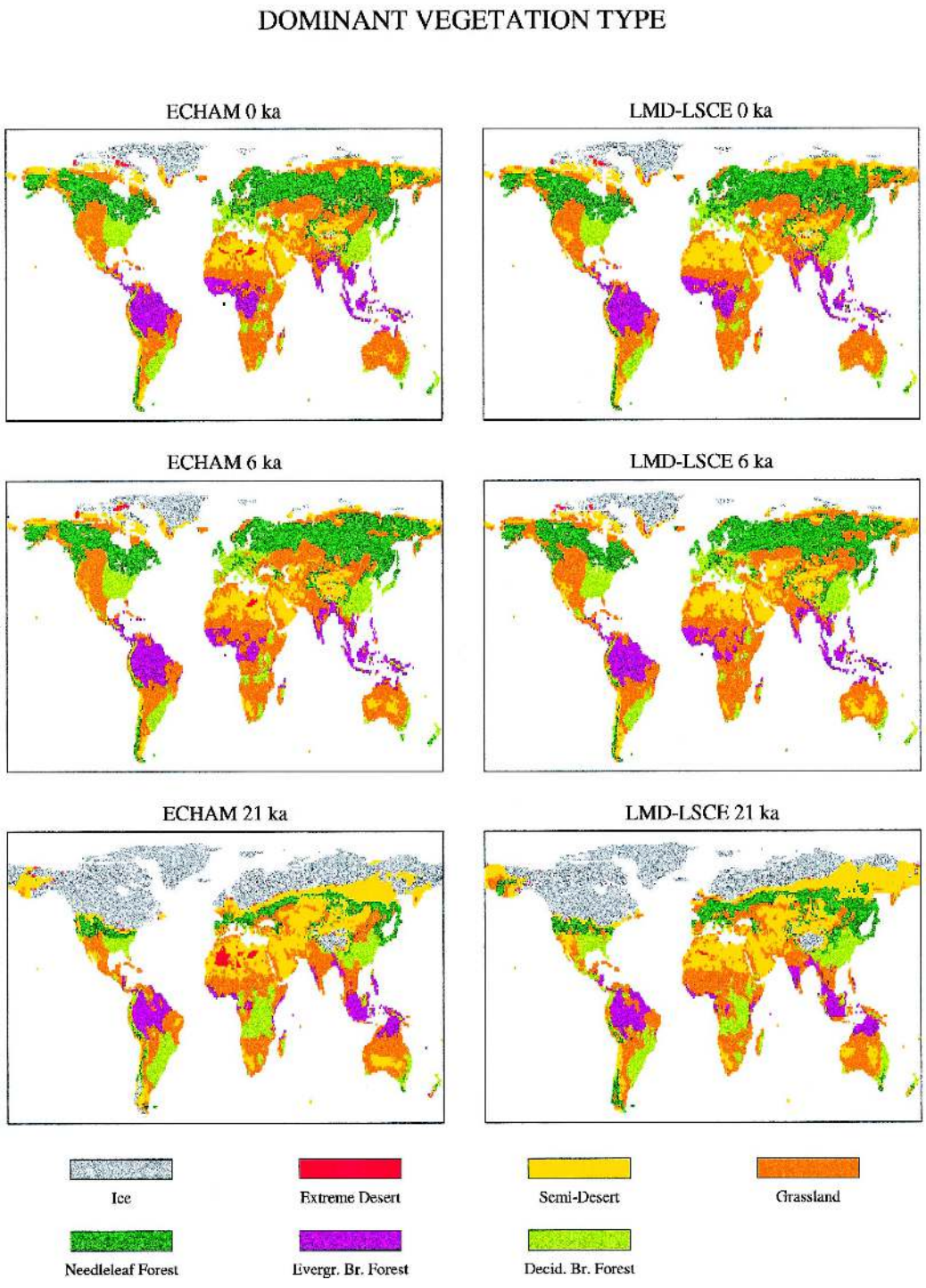

Fig. 6. Geographical distributions of the dominant (i.e., with the largest fractional area) potential vegetation type (or biome) reconstructed in the control (0 ka), the mid-Holocene (6 ka) and the LGM (21 ka) simulations by using ECHAM and LMD-LSCE «corrected» climates and by considering CO_2 fertilization.

tion. The largest areal change, however, corresponds to the buildup of the ice caps which more than offsets the increase in vegetated area associated with the sea level drop. In agreement with the global data-based reconstructions (Adams et al., 1990; van Campo et al., 1993), the area of deserts is increased in all simulations. The area of C_4 grasslands is essentially not modified, although a small increase is observed in the simulations involving CO_2 fertilization changes. The area of C_3 grasslands is reduced, but the amplitude of the decrease is strongly dependent on the CO_2 fertilization effect. Needleleaf and evergreen broadleaf forests become less widespread, while deciduous forests are expanded. It is interesting to note that the discrepancies arising from the use of different GCMs are generally smaller in grassland and semidesert ecosystems than the variations resulting from CO_2 fertilization changes.

Fig. 6 shows the geographical distribution of potential vegetation at present, mid-Holocene and LGM times as reconstructed from both ECHAM and LMD-LSCE «corrected» climates. These distributions include the effect of CO_2 fertilization. The maps report only the dominant vegetation type existing on each pixel, i.e., the biome with largest areal coverage. It must be emphasized that this mapping procedure may cause some problems, since only one vegetation type can be selected even if several types have the same fractional area. Nevertheless, these maps illustrate the main features of the changes in the distribution of the major biomes. The reduction of the evergreen broadleaf forest area at 6 ka with respect to the present mainly occurs in Africa for both GCMs. Both climatic fields also predict a reduction of the size of the Sahara desert, while in Australia desertic areas tend to be increased. At the LGM, the most striking features are the replacement of evergreen by deciduous forests in Africa, a large reduction in the size of the needleleaf forests and the increase of the desertic areas in Asia. The trends are generally consistent among the GCMs both at 6 and 21 ka. Note, however, that at LGM in northeastern China the ECHAM simulation predicts slightly more grasslands and less coniferous forests than the LMD-LSCE model. The data-based vegetation reconstruction performed for China by An et al. (1991), as reported by Peng and Apps (1997), appears to predict grasslands and no coniferous forest in this region. Another difference is the presence of needleleaf forests in southern Chile predicted in the LMD-LSCE model, instead of ice in the ECHAM simulation.

4.3. Net primary productivity

The NPP changes for the major vegetation types in the mid-Holocene or at the LGM, with respect to the present are illustrated in Fig. 7. Both the changes in the total NPP of each biome and in the NPP density (defined as the average biome NPP per unit of biome area) are reported. The amplitude of the changes is much larger at 21 ka than at 6 ka, consistent with the corresponding magnitude of the climatic perturbation.

At 6 ka, the total continental NPP is increased by 0.75–2.26 Gt C $year^{-1}$ with respect to the present if CO_2 fertilization is not taken into account (high CO_2 runs) depending on the GCM used. This increase is the net result of positive and negative contributions from the various vegetation types. The largest contribution is that from C_4 grasslands, the net productivity of which increases by 0.96 and 2.66 Gt C $year^{-1}$ in the ECHAM and LMD-LSCE simulations, respectively. In the case of ECHAM, this increase is only associated with the areal expansion of C_4 grasses, while in the LMD-LSCE run it is a combination of both an areal expansion (Fig. 5) and an increase in NPP density (Fig. 7b). As expected, when CO_2 fertilization is considered, the NPP density of C_3 vegetation is decreased with respect to the corresponding high CO_2 simulation, while C_4 NPP density is only slightly affected. Combining the changes in NPP density with those resulting from the changes in areal extent now yields a decrease (-2.70 and

Fig. 7. Changes with respect to the present of the biome NPP at the mid-Holocene (6 ka) and the LGM (21 ka) calculated by using ECHAM and LMD-LSCE «corrected» climates. The results obtained both by considering (*ECHAM* and *LMD-LSCE* runs) or neglecting (*ECHAM High* CO_2 and *LMD-LSCE High* CO_2 runs) CO_2 fertilization are illustrated. (a) Total NPP (i.e., cumulated over the biome area), (b) NPP density (i.e., per unit area).

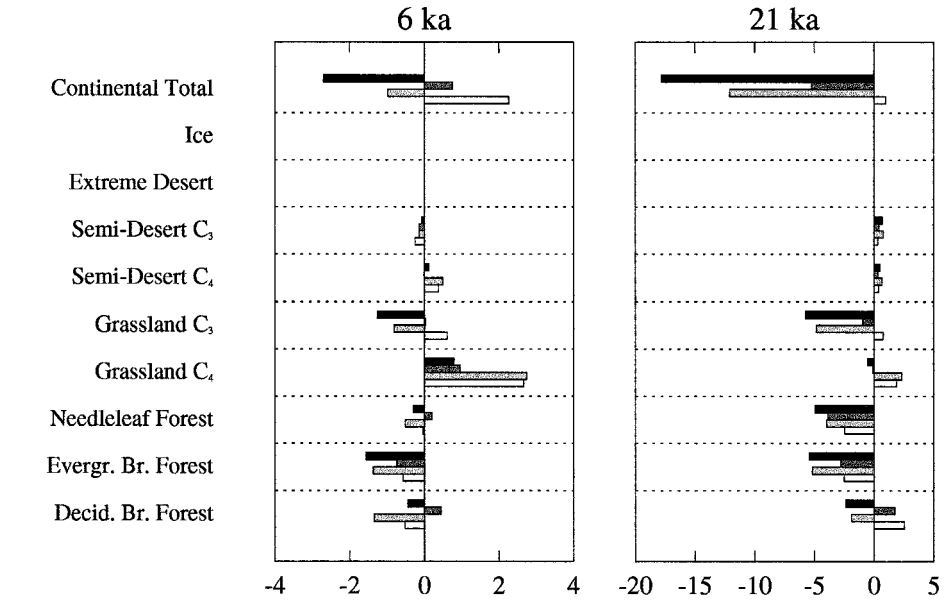
NPP (Gt C yr-1)
[Change from today]
(a)
6 ka
21 ka
Continental Total
Ice
Extreme Desert
Semi-Desert C3
Semi-Desert C4
Grassland C3
Grassland C4
Needleleaf Forest
Evergr. Br. Forest
Decid. Br. Forest
-4 -2 0 2 4
-20 -15 -10 -5 0 5

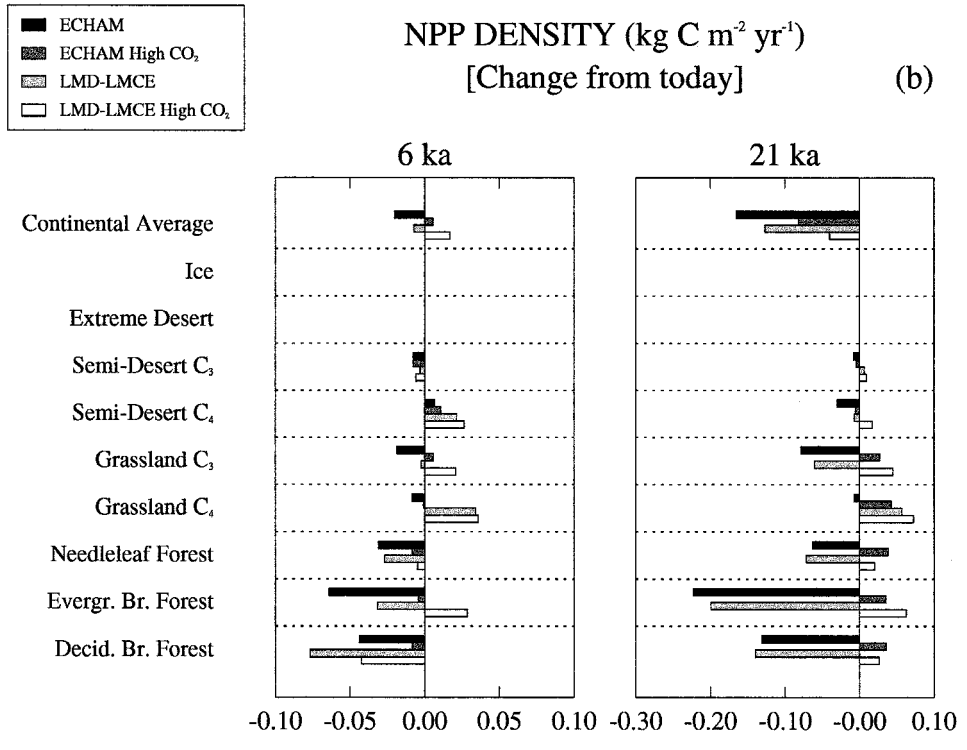
ECHAM
ECHAM High CO2
LMD-LMCE
LMD-LMCE High CO2
NPP DENSITY (kg C m-2 yr-1)
[Change from today]
(b)
6 ka
21 ka
Continental Average
Ice
Extreme Desert
Semi-Desert C3
Semi-Desert C4
Grassland C3
Grassland C4
Needleleaf Forest
Evergr. Br. Forest
Decid. Br. Forest
-0.10 -0.05 0.00 0.05 0.10
-0.30 -0.20 -0.10 -0.00 0.10

-0.98 Gt C year^{-1} for ECHAM and LMD-LSCE simulations, respectively) in the total continental NPP at 6 ka with respect to the present. The CO_2 fertilization effect on global NPP thus overcompensates for the climatic response, despite the relatively small variation (20 ppmv) in atmospheric CO_2 levels. Only C_4 biomes now see their productivities increase with respect to the present. The largest NPP decrease is observed for evergreen broadleaf forests, for which both climate and CO_2 fertilization act to reduce productivity.

In the high CO_2 (280 ppmv) simulations for 21 ka, the total continental NPP is reduced with respect to the present by 4.94 Gt C year^{-1} for ECHAM and increased by 0.98 Gt C year^{-1} for LMD-LSCE. These NPP variations are the result of both the climatic changes and the increased land area. On average, however, the increase in the ice cap area exceeds the area of emerged shelf (Fig. 5), so that the vegetated area was smaller at LGM than today. As a result, the increased total continental NPP obtained in the LMD-LSCE (High CO_2) simulation necessarily implies that, per unit area, the biomes were on average more productive at LGM than today, suggesting that biomes were confined into regions which were climatically slightly more favorable to their development. This is indeed confirmed by Fig. 7b where it is shown that all nondesertic biomes have a higher NPP density at the LGM that at present in all high CO_2 simulations. This unexpected result is not only observed in the LMD-LSCE, but also in the ECHAM high CO_2 simulation. The reason for this increase is not easy to understand, since the response of NPP to the climate is highly non linear and moreover not only the annual average of climatic variable is important, but their seasonal variations (which may, for instance, induce changes in growing season length). Nevertheless, it appears that some biomes, such as C_3 grasslands or deciduous broadleaf forests, are on average found in slightly warmer (0.1 to 3.5°C depending on the biome and the GCM) regions at LGM than today due to their migration over the continents. Soil water available for plant growth is generally lower for most biomes except deserts. However, the most striking feature, which may explain the higher NPP density of biomes, is the substantial reduction of cloud cover (by 2–16%) at LGM and the corresponding increase of solar irradiance. This increase in solar irradiance explains the general reduction of soil water through increased evapotranspiration. This decrease of soil water acts to decrease productivity in water-limited regions, but apparently at the biome scale this effect of soil water reduction is offset by the direct stimulation of photosynthesis by the increased solar irradiance. Although quite possible, this effect is probably model-dependent and it would be interesting to perform similar experiments with other biospheric models. Since several biomes see their areas decrease, the increased NPP densities of biomes does not necessarily translate into a higher total continental NPP, but may lead into a decrease as observed for the ECHAM climate. When CO_2 fertilization is considered (the atmospheric CO2 level changing from 280 to 200 ppmv), the NPP densities of most biomes now tend to be reduced at LGM with respect to their present values, illustrating again the potential importance of the CO_2 fertilization effect. Under these conditions, total continental NPP is decreased by 17.80 and 12.09 Gt C year^{-1} at LGM with respect to the present in ECHAM and LMD-LSCE simulations, respectively. These are really substantial changes of continental NPP.

4.4. Total carbon stock

The changes in total carbon stocks (i.e., living phytomass, litter and soil carbon) are illustrated in Fig. 8. Again, both the total stocks and the densities are reported. These changes in total carbon stocks mirror those in NPP: if NPP increases, the total carbon stock is also expected to increase. Nevertheless, the results may also depend on the direct response of the carbon stocks to climate. For example,

Fig. 8. Changes with respect to the present of the biome total carbon stocks (vegetation + litter + soil) at the mid-Holocene (6 ka) and the LGM (21 ka) calculated by using ECHAM and LMD-LSCE «corrected» climates. The results obtained both by considering (*ECHAM* and *LMD-LSCE* runs) or neglecting (*ECHAM High* CO_2 and *LMD-LSCE High* CO_2 runs) CO_2 fertilization are illustrated. (a) Total carbon stock (i.e., cumulated over the biome area), (b) Total carbon density (i.e., per unit area).

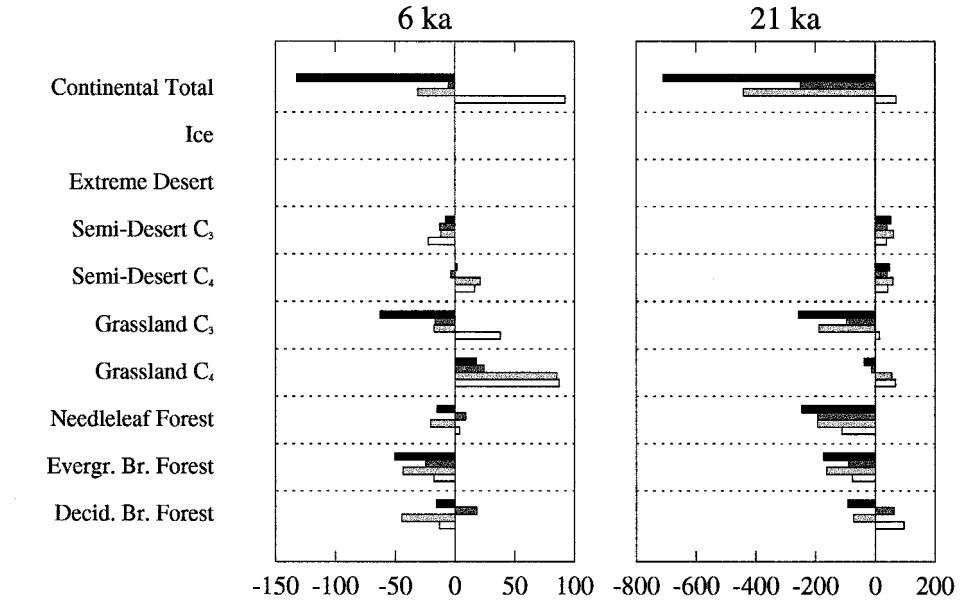
TOTAL CARBON (Gt C)
[Change from today]
(a)
6 ka
21 ka
Continental Total
Ice
Extreme Desert
Semi-Desert C3
Semi-Desert C4
Grassland C3
Grassland C4
Needleleaf Forest
Evergr. Br. Forest
Decid. Br. Forest
-150 -100 -50 0 50 100
-800 -600 -400 -200 0 200

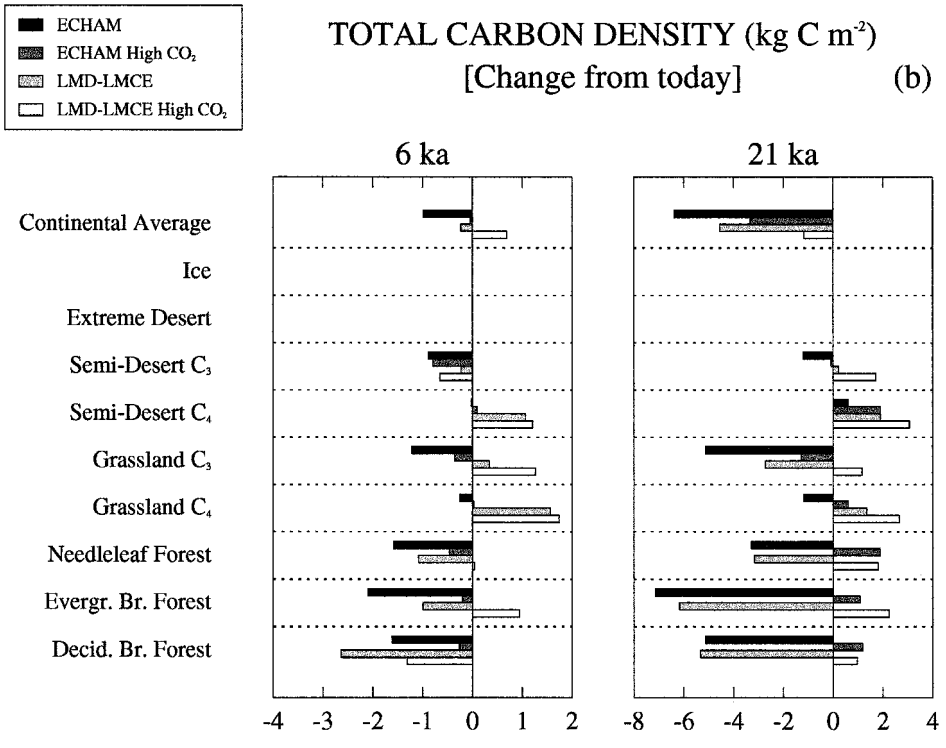
ECHAM
ECHAM High CO2
LMD-LMCE
LMD-LMCE High CO2
TOTAL CARBON DENSITY (kg C m-2)
[Change from today]
(b)
6 ka
21 ka
Continental Average
Ice
Extreme Desert
Semi-Desert C3
Semi-Desert C4
Grassland C3
Grassland C4
Needleleaf Forest
Evergr. Br. Forest
Decid. Br. Forest
-4 -3 -2 -1 0 1 2
-8 -6 -4 -2 0 2 4

at lower temperatures the residence time of soil carbon will be longer, so that the soil carbon stock can be expected to increase. The trends in the total amounts of carbon stored in the various biomes (Fig. 8a) appear relatively consistent among the simulations corresponding to both GCMs. The carbon stock of C_3 vegetation is generally lower at 6 or 21 ka than at present, while the C_4 stock tends to be higher. This trend is particularly marked in the simulations involving CO_2 fertilization. The change with respect to the present in the total continental carbon stock varies from -132 to $+92$ Gt C at 6 ka and from -710 to $+70$ Gt C at 21 ka, depending on the simulation considered.

According to our model, the carbon density of a given biome (Fig. 8b) is far from being constant (as sometimes assumed in some simple reconstructions of past carbon stocks). At 21 ka, for instance, an increase in carbon density of 1–2 kg C m^{-2} is observed for most biomes when CO_2 fertilization is neglected, while when it is considered decreases of 2–6 kg C m^{-2} are often reached.

4.5. ^{13}C isotopic fractionation

In the control biospheric simulation (for preindustrial times), the calculated fractionation of the global vegetation is -16.39‰ for ECHAM and -16.55‰ for LMD-LSCE (Table 2). These numbers corresponds to the weighted average between C_3 and C_4 ecosystems in the model. With a value of -6.5‰ for the isotopic composition of the preindustrial atmosphere (Friedli et al., 1986), they imply that the global $\delta^{13}C$ of the land biosphere was -22.89 and -23.05‰ for ECHAM and LMD-LSCE, respectively, before the industrial revolution. These global biospheric $\delta^{13}C$ are relatively high. In this control run, the model ^{13}C fractionation of forest biomes fall between -20.2 and -20.8‰. These numbers correspond to a preindustrial $\delta^{13}C$ of forest biomass in the range of -26.7 to -27.3‰. These results fully agree with the data of Bird et al. (1996) which, after correction for the industrial perturbation, indicate a -27‰ $\delta^{13}C$ value of preindustrial soils under non water-stressed C_3 vegetation. The relatively high value of the global biospheric $\delta^{13}C$ estimated here may thus be linked to an slight overestimation of the C_4 biomass, possibly due to the fact that C_4 material in soils tend to decompose more rapidly than C_3 one (Bird and Pousai, 1997), an effect which was not included in our model.

As discussed in Section 4.4, the calculated amount of C_4 biomass in vegetation and soils were larger than at present at the mid-Holocene and the LGM, while the reverse trend is obtained for C_3 vegetation. Consequently, the fraction of C_4 biomass in total continental carbon was significantly larger in the past. This result is illustrated in Fig. 9 showing the geographical distribution of the fraction of C_4 carbon in the vegetation–soil reservoir (named here C_4 biomass fraction) in all of the simulations taking CO_2 fertlization into account. As obvious from this figure, C_4 vegetation expanded at 6 and 21 ka in peri-desertic regions. Over northeastern China at 21 ka, this C_4 expansion is slightly more important in the ECHAM than in the LMD-LSCE simulation. This difference arises from the reconstruction of grasslands by ECHAM where the LMD-LSCE model predicts forest ecosystems. The global values of the C_4 biomass fraction are also reported in Fig. 9. The change in this global fraction from the present to the mid-Holocene is much smaller in ECHAM than in LMD-LSCE, while the magnitudes of the changes are comparable for the LGM. At 21 ka in ECHAM, C_4 material contribute to global biospheric carbon for as much as 33%. The difference with respect to the present value (21%) is due partly to the climatic change and partly to CO_2 fertilization, the intermediate ECHAM High CO_2 simulation yielding 26% of C_4 carbon.

These changes in the fraction of C_4 biomass are reflected in the changes of the continental average of the biospheric ^{13}C fractionation displayed in Fig. 10. Indeed higher (i.e., less negative) global values of the ^{13}C fractionation are obtained at 6 and 21 ka, due mainly to the larger contribution of C_4 photosynthe-

Fig. 9. Geographical distributions of the fraction of C_4 carbon in the vegetation–litter–soil biomass pool calculated in the control (0 ka), the mid-Holocene (6 ka) and the LGM (21 ka) simulations by using ECHAM and LMD-LSCE «corrected» climates and by considering CO_2 fertilization.

C_4 BIOMASS FRACTION (VEGETATION+LITTER+SOIL)

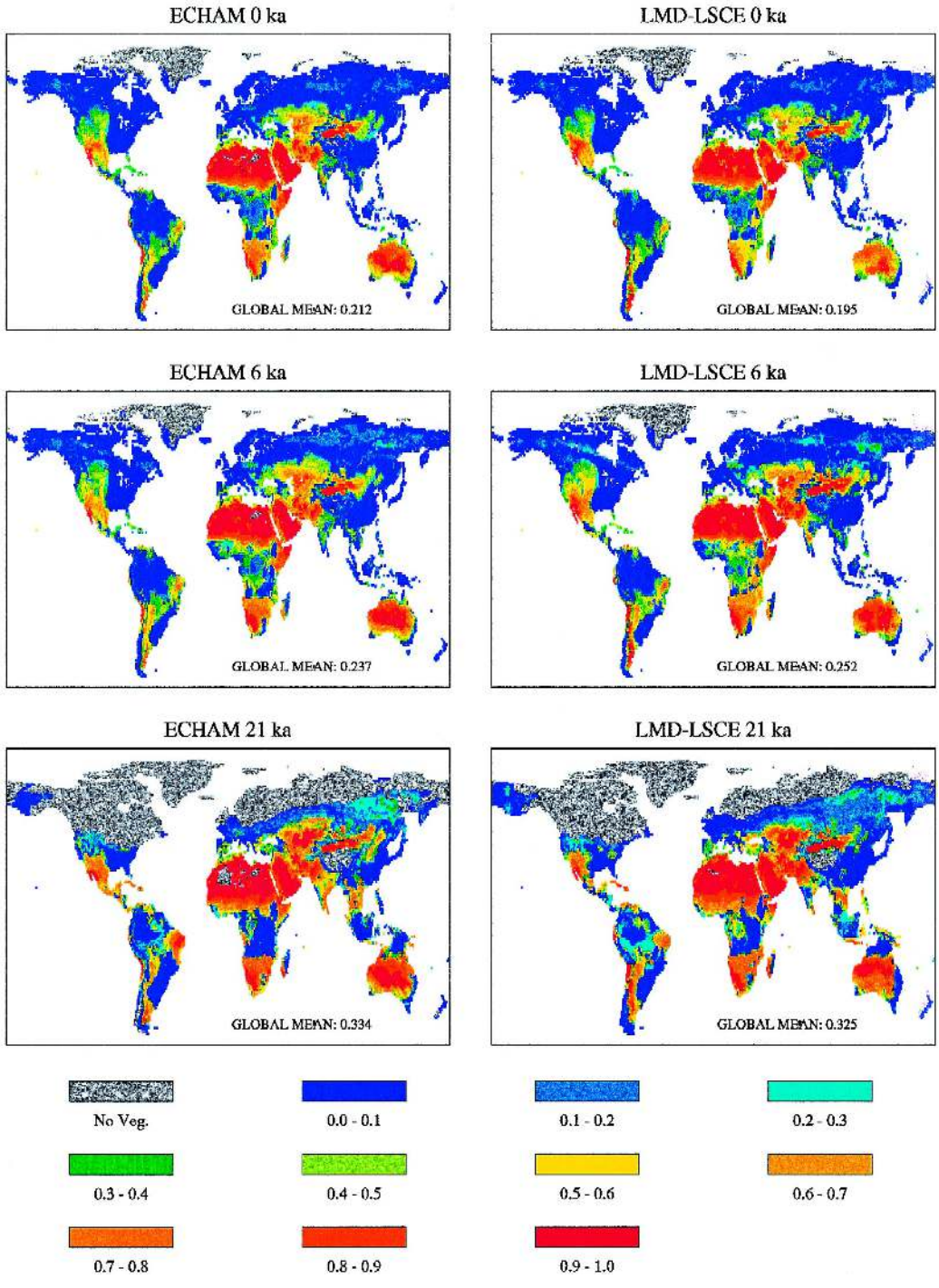

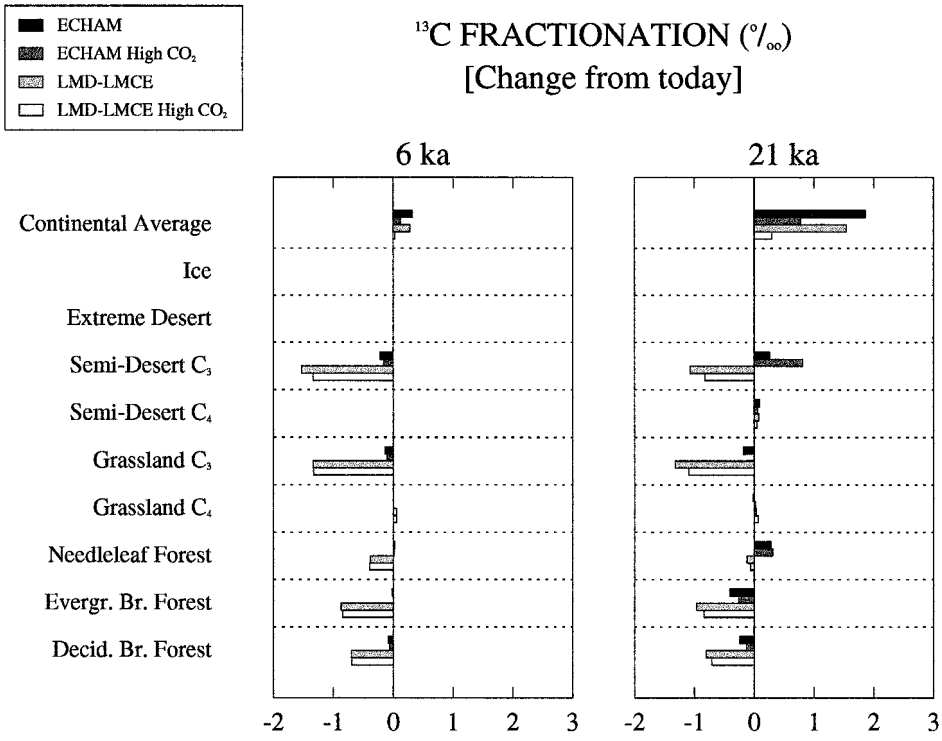

Fig. 10. Changes with respect to the present of the average ^{13}C fractionation of the biomes at the mid-Holocene (6 ka) and the LGM (21 ka) calculated by using ECHAM and LMD-LSCE «corrected» climates. The results obtained both by considering (*ECHAM* and *LMD-LSCE* runs) or neglecting (*ECHAM High* CO_2 and *LMD-LSCE High* CO_2 runs) CO_2 fertilization are illustrated. Note that the continental average values are the biomass-weighted means of the different biome fractionations. The positive shifts obtained for these continental averages are largely the result of larger fractions C_4 biomass at 6 and 21 ka.

sis the fractionation of which is close to -4‰ (instead of -21 to -17‰ for C_3 photosynthesis). This change in the relative amount of C_4 vegetation is the dominant factor in the regulation of the ^{13}C fractionation variations from the past to the present. However, the ^{13}C fractionation of both photosynthetic pathways are also modified due to changes in the ratio c_i/c_a between the CO_2 pressures in the intercellular medium and in the atmosphere. This effect is negligible for C_4 ecosystems. However, as shown in Fig. 10, the average fractionation of C_3 biomes are substantially affected by this process. The response of the biospheric model in this respect is highly dependent on the used GCM climate. In ECHAM simulations, both positive and negative changes of the fractionation of C_3 biomes may be found and their magnitudes remain lower than 0.5‰, while the LMD-LSCE predicted changes are always negative (i.e., towards more negative values) ranging from -0.4 to -1.5‰. The effect of these changes on the global average biospheric ^{13}C fractionation is opposite to that of the variations in the relative fraction of C_4 biomass. Note also that ^{13}C fractionation by C_3 vegetation is only weakly dependent on the CO_2 fertilization effect, although the modification of stomatal regulation with changing atmospheric CO_2 pressure is considered by the model. The results obtained here must, nevertheless, be regarded as very preliminary, since the relative air humidity is held constant from the past to the present in the various simulations, while relative humidity is an important factor governing stomatal regulation and hence the intercellular CO_2 pressure and the ^{13}C isotopic discrimination.

Table 3 synthesizes the various results obtained here for the changes in the total carbon and the average ^{13}C fractionation of the land biosphere from 6 and 21 ka to the present. Using this information

Table 3
Changes with respect to the present (i.e., preindustrial) in total carbon stock and average ^{13}C fractionation of the land biosphere calculated in the various simulations performed for the mid-Holocene (6 ka) and the LGM (21 ka)

Time period (ka)	Simulation	Total carbon change (Gt C)	^{13}C Fractionation change (‰)	Oceanic $\delta^{13}C$ change (‰)
6	ECHAM	−132	+0.32	−0.10
	ECHAM High CO_2	−5	+0.12	−0.02
	LMD-LSCE	−31	+0.28	−0.04
	LMD-LSCE High CO_2	+92	+0.03	+0.05
21	ECHAM	−710	+1.86	−0.47
	ECHAM High CO_2	−250	+0.78	−0.18
	LMD-LSCE	−441	+1.54	−0.32
	LMD-LSCE High CO_2	+70	+0.30	+0.03

The implied changes of the average oceanic $\delta^{13}C$ with respect to the present are also listed. The calculation of the oceanic carbon isotopic composition was performed by assuming no change in the total ^{12}C and ^{13}C inventories of the ocean-atmosphere-biosphere system. Present-day reference values for the biospheric carbon stocks and the ^{13}C fractionation may be found in Table 2 for both sets of GCM climates. Values of 600 Gt C, 557 Gt C and 429 Gt C, and of −6.5‰ (preindustrial value, Friedli et al., 1986), −6.5‰ (taken equal to preindustrial) and −7.0‰ (Leuenberger et al., 1992) are assumed for the carbon stocks and $\delta^{13}C$ of the atmosphere at present, 6 and 21 ka, respectively. The present-day carbon stock and $\delta^{13}C$ of the ocean are taken as 39,000 Gt C and 0‰, respectively.

together with the present-day sizes and isotopic compositions of the ocean and atmosphere and considering the ocean–atmosphere–biosphere system to be closed (i.e., neglecting the exchanges with the sediments and the crustal rocks), it is possible to evaluate the changes in the oceanic carbon isotopic composition from the LGM or the mid-Holocene to the present (e.g., Bird et al., 1994; François et al., 1998). Table 3 lists the changes in oceanic $\delta^{13}C$ calculated in this way for all of the simulations performed here for 6 and 21 ka. Values ranging between −0.47 and +0.03‰ are obtained for the difference between the LGM and the present. These values can be compared to the estimates from the global average of the oceanic isotopic data recorded in carbonates which suggests values of −0.32‰ (Duplessy et al., 1988) or −0.40‰ (Crowley, 1995). The values found here in the simulations taking CO_2 fertilization into account (−0.47‰ for ECHAM and −0.32‰ for LMD-LSCE) compare well with these oceanic data. In contrast, the model values obtained by neglecting CO_2 fertilization appear to be lower than the measured values. Note, however, that if the dependence of foraminiferal $\delta^{13}C$ on seawater carbonate ion concentration (Spero et al., 1997) were taken into account, the «true» increase of the global oceanic $\delta^{13}C$ between the LGM and the present would be strongly reduced with respect to the above «apparent» value of 0.32–0.40‰ and might become more consistent with our results obtained by neglecting CO_2 fertilization! The oceanic $\delta^{13}C$ change from the mid-Holocene to the present calculated here is substantially smaller than for the LGM. The changes calculated here for the oceanic isotopic composition consider the effects of the variations in both the total carbon stock and the average ^{13}C fractionation of the continental biosphere. Although the variation in the carbon stock is clearly the most important factor, the change in the isotopic fractionation contributes for −0.061‰ in the total −0.47‰ variation calculated in the ECHAM simulation for LGM. The corresponding contribution is −0.060‰ in the LMD-LSCE −0.32‰ change. Consequently, the contribution of the isotopic fractionation change may reach 13–19% of the total signal and hence is not negligible.

5. Conclusion

In this study, we performed model reconstructions of the biosphere at mid-Holocene and LGM times. These reconstructions used the CARAIB biosphere model, forced with climatic fields from two different GCMs. The biospheric model used corrected climates, in which only the anomalies of the climatic fields calculated by the GCMs are taken into account. We showed that the trends predicted on the

basis of both GCM climates are broadly consistent with each other, although discrepancies in the magnitude of the changes may sometimes be relatively large. These discrepancies between the results obtained with different GCM climates are usually smaller than the differences between the biospheric runs performed while considering or neglecting the CO_2 fertilization effect. This result highlights the potential importance of CO_2 fertilization. Indeed, the important role of CO_2 fertilization is even true at 6 ka for which the change in the atmospheric CO_2 level with respect to preindustrial times is only of 20 ppmv. However, the magnitude of the land biosphere response to the CO_2 fertilization calculated here is probably overestimated, since CARAIB does not consider the nutrient cycles (especially nitrogen) and the response may be expected to be reduced in nutrient-depleted regions.

The results for the mid-Holocene suggest a northward shift of the needleleaf forest in the boreal region and an expansion of C_4 grasslands on the border of the Sahara Desert, in good agreement with the model study by Foley (1994) and with paleobotanical evidence (Ritchie et al., 1983; Khotinsky, 1984; Street-Perrott and Perrott, 1993). However, our simulations only show an increase of global NPP (by 1–4%) comparable with the results obtained by Foley (1994) when the CO_2 fertilization is neglected. Otherwise, global NPP decreases (by 2–5%) together with the global carbon stock.

For the last glacial maximum, the models show an expansion of deserts and semideserts and a reduction of needleleaf and evergreen broadleaf forests consistent with the data-based reconstructions (Adams et al., 1990; van Campo et al., 1993), but predicts a substantial decrease of the total grassland area in conflict with the same data-based estimates. The changes in global NPP vary from an increase by 1.7% at LGM with respect to the present in the LMD-LSCE simulation neglecting CO_2 fertilization to a decrease by 30% in the ECHAM simulation considering CO_2 fertilization. The resulting range of carbon stock variations ($+70$ to -710 Gt C at LGM relative to present) approximately reproduces the whole range of previous GCM-based estimates (Prentice and Fung, 1990; Friedlingstein et al., 1992; Prentice et al., 1993; Esser and Lautenschlager, 1994; Friedlingstein et al., 1995; François et al., 1998).

The changes in climate and atmospheric CO_2 at the mid-Holocene and last glacial maximum with respect to the present also induce changes in the relative amount of C_4 vs. C_3 vegetation. At both time periods, C_4 vegetation was relatively more widespread from a biomass point of view than at present. As a result, the ^{13}C fractionation of the biosphere was altered towards a reduced isotopic discrimination by photosynthesis (i.e., less negative fractionation). This ^{13}C fractionation change associated with the variations in the C_3/C_4 distribution was partly compensated by an opposite change of smaller magnitude in the fractionation of C_3 vegetation. The total fractionation change appears to significantly alter the ^{13}C budget of the biosphere and hence of the ocean–atmosphere system, although the changes in the biospheric carbon stock still prevail in controlling the variations of the oceanic $\delta^{13}C$ from the past to the present.

A series of model refinements may improve the results obtained here. Firstly, the relative distribution of forests and grasslands predicted by the bioclimatic scheme does not depend on the CO_2 fertilization effect. For this reason, forested areas in the past are overestimated at the expense of grasslands. The consideration of NPP ratios in the prediction of all vegetation types, as done here for the C_3/C_4 distribution, would probably lead to a relative distribution of forests and grasslands closer to that suggested by the data-based reconstructions (especially for the LGM vegetation). Secondly, the results are probably very sensitive to the way the interactions between the carbon and the water cycles are described in the model. In particular, relative air humidity does not vary from the past to the present in the biospheric simulations presented here. This approximation may alter the calculated values of ^{13}C fractionation, as well as of the NPP and carbon stocks. Thirdly, the response of vegetation to environmental changes depends on other biogeochemical cycles than water and carbon. More specifically, the consideration of the nitrogen cycle may substantially reduce the CO_2 fertilization effect shown here to have been potentially important in the regulation of past vegetation changes. Finally, coupling the biome prediction scheme (and probably the whole biospheric model) with the GCM may also significantly alter the reconstruction of both past vegetation and climate. Such a

coupling has, for instance, been shown to be important in simulating the northward vegetation shift in southern Sahara at mid-Holocene times (Kutzbach et al., 1996) or the onset of glaciations 115 ka ago (de Noblet et al., 1996; Gallimore and Kutzbach, 1996). Future model reconstructions of past vegetation should converge towards the use of such coupled models describing more completely the dynamics of the climate-biosphere system.

Acknowledgements

LMF is supported by the Belgian Foundation for Scientific Research (F.N.R.S.) and PW by the Commission of the European Union under contract ENV4-CT95-0111 (*ESCOBA-Biosphere*) within the *Environment and Climate* Programme, and by the *Sustainable Development* Programme of the Belgian Office for Scientific, Technical and Cultural Affairs (contract CG/DD/11A). Funding for research costs by F.N.R.S. is also gratefully acknowledged. We thank P. Friedlingstein for making the code of his bioclimatic scheme available to us.

References

Adams, J.M., Faure, H., Faure-Denard, L., McGlade, J.M., Woodward, F.I., 1990. Increases in the terrestrial carbon storage from the Last Glacial Maximum to the present. Nature 348, 711–714.

An, Z.S., Wu, X., Lu, Y., Zhang, D., Sun, X., Dong, G., 1991. A preliminary study of the paleoenvironment changes of China during the last 20,000 years. In: Liu, D.S. (Ed.), Quaternary Geology and Global Change. Beijing, China, pp. 1–26, in Chinese.

Ball, J.T., Woodrow, I.E., Berry, J.A., 1987. A model predicting stomatal conductance and its contribution to the control of photosynthesis under different environmental conditions. In: Bigins, J. (Ed.), Progress in Photosynthesis Research, Vol. 4. Nijhoff, Dordrecht, pp. 221–224.

Barnola, J.-M., Raynaud, D., Korotkevich, Y.S., Lorius, C., 1987. Vostok ice core provides 160,000-year record of atmospheric CO_2. Nature 329, 408–414.

Berger, W.H., Keir, R.S., 1984. Glacial-Holocene changes in atmospheric CO_2 and the deep-sea record. In: Hansen, J.E., Takahashi (Eds.), Climate Processes and Climate Sensitivity. Geophys. Monogr. Ser., Vol. 29. American Geophysical Union, Washington DC, pp. 337–351.

Bird, M.I., Pousai, P., 1997. Variations of $\delta^{13}C$ in surface soil organic carbon pool. Global Biogeochemical Cycles 11, 313–322.

Bird, M.I., Lloyd, J., Farquhar, G.D., 1994. Terrestrial carbon storage at the LGM. Nature 371, 566.

Bird, M.I., Chivas, A.R., Head, J., 1996. A latitudinal gradient in carbon turnover times in forest soils. Nature 381, 143–146.

Broecker, W.S., 1982. Ocean chemistry during glacial times. Geochim. Cosmochim. Acta 46, 1689–1705.

Broecker, W.S., Peng, T.-H., 1989. The cause of the glacial to interglacial atmospheric CO_2 change: a polar alkalinity hypothesis. Global Biogeochemical Cycles 3, 215–239.

Chalita, S., le Treut, H., 1994. The albedo of temperate and boreal forests and the Northern hemisphere climate: a sensitivity experiment using the LMD AGCM. Climate Dynamics 10, 231–240.

CLIMAP Project Members, 1976. The surface of the ice-age Earth. Science 191, 1131–1137.

CLIMAP Project Members, 1981. Seasonal reconstruction of the earth's surface at the last glacial maximum. Geol. Soc. America Map Chart Ser., MC-36, Geol. Soc. Am., Boulder, CO.

Collatz, G.J., Ribas-Carbo, M., Berry, J.A., 1992. Coupled photosynthesis-stomatal conductance model for leaves of C_4 plants. Aust. J. Plant Physiol. 19, 519–538.

Crowley, T.J., 1995. Ice age terrestrial carbon changes revisited. Global Biogeochemical Cycles 9, 377–389.

de Noblet, N., Prentice, I.C., Joussaume, S., Texier, D., Botta, A., Haxeltine, A., 1996. Possible role of atmosphere–biosphere interactions triggering the last glaciation. Geophys. Res. Lett. 23, 3191–3194.

DKRZ, 1994. The Atmospheric General Circulation Model. Technical Report 6, Modellbetreuungsgruppe, Deutsches Klimarechenzentrum, Hamburg.

Ducoudré, N., Laval, K., 1993. SECHIBA a new set of parametrization of the hydrologic exchanges at the land atmosphere interface within the LMD AGCM. Journal of Climate 6, 249–273.

Dümenil, L., Todini, E., 1992. A rainfall runoff scheme for use in the Hamburg climate model. In: O'Kane, J.P. (Ed.), Advances in Theoretical Hydrology, A Tribute to James Dooge. European Geophysical Society Series of Hydrological Sciences, Vol. 1. Elsevier, Amsterdam, pp. 129–157.

Duplessy, J.-C., Shackleton, N.J., Fairbanks, R.G., Labeyrie, L., Oppo, D., Kallel, N., 1988. Deep water source variations during the last climatic cycle and their impact on the global deepwater circulation. Paleoceanography 3, 343–360.

Esser, G., Lautenschlager, M., 1994. Estimating the change of carbon in the terrestrial biosphere from 18,000 bp to present using a carbon cycle model. Environ. Pollut. 83, 45–53.

Farquhar, G.D., von Caemmerer, S., Berry, J.A., 1980. A biogeochemical model of photosynthetic CO_2 assimilation in leaves of C_3 species. Planta 149, 78–90.

Foley, J., 1994. The sensitivity of the terrestrial biosphere to climate change: a simulation of the middle Holocene. Global Biogeochemical Cycles 8, 505–525.

Fouquart, Y., Bonnel, B., 1980. Computations of solar heating of the Earth atmosphere: a new parametrization. Beitr. Phys. Atmos. 53, 35.

François, L.M., Delire, C., Warnant, P., Munhoven, G., 1998. Modelling the glacial–interglacial changes in the continental biosphere. Global Planet. Change 16–17, 37–52.

Friedli, H., Loetscher, H., Oeschger, H., Siegenthaler, U., Stauffer, B., 1986. Ice core record of the $^{13}C/^{12}C$ ratio of atmospheric CO_2 in the past two centuries. Nature 324, 237–238.

Friedlingstein, P., Delire, C., Müller, J.-F., Gérard, J.-C., 1992. The climate-induced variation of the continental biosphere: a model simulation of the Last Glacial Maximum. Geophys. Res. Lett. 19, 897–900.

Friedlingstein, P., Prentice, K.C., Fung, I.Y., John, J.G., Brasseur, G.P., 1995. Carbon–biosphere–climate interactions in the last glacial maximum. J. Geophys. Res. 100, 7203–7221.

Gallimore, R.G., Kutzbach, J.E., 1996. Role of orbitally induced changes in tundra area in the onset of glaciation. Nature 381, 503–505.

Gates, W.L., 1992. The Atmospheric Model Intercomparison Project (AMIP). Bull. Am. Meteorol. Soc. 73, 1962–1970.

Gates, W.L., Nelson, A.B., 1975. A new, revised, tabulation of the Scripps topography on a 1 degree global grid. The Rand. R-1276-1-ARPA.

Geleyn, J.F., Preuss, H.J., 1983. A new data set of satellite-derived surface albedo values for operational use at ECMWF. Arch. Meteor. Geophys. Bioclim., Ser. A 32, 353–359.

Gibbs, M.T., Kump, L.R., 1994. Global chemical erosion during the last glacial maximum and the present: sensitivity to changes in lithology and hydrology. Paleoceanography 9, 529–543.

Hense, A., Kerschgens, M., Raschke, E., 1982. An economical method for computing radiative transfer in circulation models. Q. J. R. Meteor. Soc. 108, 231–252.

Hubert, B., François, L.M., Warnant, P., Strivay, D., 1998. Stochastic generation of meteorological variables and effects on global models of water and carbon cycles in vegetation and soils. J. Hydrol., 212–213, 318–334.

Hunt, E.R. Jr., Piper, S.C., Nemani, R., Keeling, C.D., Otto, R.D., Running, S.W., 1996. Global net carbon exchange and intra-annual atmospheric CO_2 concentrations predicted by an ecosystem process model and three-dimensional atmospheric transport model. Global Biogeochemical Cycles 10, 431–456.

Joussaume, S., Taylor, K., 1995. Status of the paleoclimate Modeling Intercomparison Project. In: Gates, W.L. (Ed.), Proceedings of the First International AMIP Scientific Conference, WCRP-92, pp. 415–430.

Jouzel, J., Barkov, N.I., Barnola, J.M., Bender, M., Chapellaz, J., Genthon, C., Kotlyakov, V.M., Lipenkov, V., Lorius, C., Petit, J.-R., Raynaud, D., Raisbeck, G., Ritz, C., Sowers, T., Stievenard, M., Yiou, F., Yiou, P., 1993. Extending the Vostok ice-core record of palaeoclimate to the penultimate glacial period. Nature 364, 407–412.

Khotinsky, N.A., 1984. Holocene vegetation history. In: Velichko, A.A., Wright, J.H.E., Barnosky, C.W. (Eds.), Late Quaternary Environments of the Soviet Union. University of Minnesota Press, Minneapolis, pp. 179–200.

Knox, F., McElroy, M.B., 1984. Changes in atmospheric CO_2: influence of the marine biota at high latitude. J. Geophys. Res. 89, 4629–4637.

Kuo, H.L., 1965. On formation and intensification of tropical cyclones through latent heat release by cumulus convection. J. Atmos. Sci. 22, 1482–1497.

Kutzbach, J., Bonan, G., Foley, J., Harrison, S.P., 1996. Vegetation and soil feedbacks on the response of the African monsoon to orbital forcing in the early to middle Holocene. Nature 384, 623–626.

Landsberg, J.J., 1986. Physiological Ecology of Forest Production. Academic Press, London.

Leemans, R., Cramer, W.P., 1991. The IIASA database for mean monthly values of temperature, precipitation and cloudiness on a global terrestrial grid. IIASA-Report RR-91-18, International Institute for Applied Systems Analysis, Laxenburg, Austria.

Leuenberger, M., Siegenthaler, U., Langway, C.C., 1992. Carbon isotope composition of atmospheric CO_2 during the last ice age from an Antarctic ice core. Nature 357, 488–490.

Martin, J.H., 1990. Glacial–interglacial CO_2 changes: the iron hypothesis. Paleoceanography 5, 1–13.

Mitchell, J.F.B., Grahame, N.S., Needham, K.H., 1988. Climate simulations for 9000 years before present: seasonal variations and effect of the Laurentide ice sheet. J. Geophys. Res. 93, 8283–8303.

Morcrette, J.-J., 1991. Radiation and cloud radiative properties in the ECMWF operational weather forcast model. J. Geophys. Res. 96, 9121–9132.

Munhoven, G., François, L.M., 1996. Glacial–interglacial variability of atmospheric CO_2 due to changing continental silicate rock weathering: a model study. J. Geophys. Res. 101, 21423–21437.

Nemry, B., François, L.M., Warnant, P., Robinet, F., Gérard, J.-C., 1996. The seasonality of the CO_2 exchange between the atmosphere and the land biosphere: a study with a global mechanistic model. J. Geophys. Res. 101, 7111–7125.

O'Leary, M.H., 1993. Biochemical basis of carbon isotope fractionation. In: Ehleringer et al., J.R. (Eds.), Stable Isotopes and Plant Carbon–Water Relations. Academic Press, San Diego, CA, pp. 19–28.

Opdyke, B.N., Walker, J.C.G., 1992. Return of the coral reef hypothesis: basin to shelf partitioning of $CaCO_3$ and its effect on atmospheric CO_2. Geology 20, 733–736.

Peltier, W.R., 1994. Ice age paleotopography. Science 265, 195–201.

Peng, C., Apps, M., 1997. Contribution of China to the global carbon cycle since the last glacial maximum: reconstruction from palaeovegetation maps and an empirical biosphere model. Tellus 49B, 393–408.

Prentice, K.C., Fung, I.Y., 1990. The sensitivity of terrestrial carbon storage to climate change. Nature 346, 48–51.

Prentice, I.C., Cramer, W., Harrison, S.P., Leemans, R., Monserud, R.A., Solomon, A.M., 1992. A global biome model based on plant physiology and dominance, soil properties and climate. J. Biogeogr. 19, 117–134.

Prentice, I.C., Sykes, M.T., Lautenschlager, M., Harrison, S.P., Dennissenko, O., Bartlein, P.J., 1993. Modelling the global vegetation patterns and terrestrial carbon storage at the last glacial maximum. Global Ecol. Biogeogr. Lett. 3, 67–76.

Raich, J.W., Schlesinger, W.H., 1992. The global carbon dioxide flux in soil respiration and its relationship to vegetation and climate. Tellus 44B, 81–89.

Raich, J.W., Rastetter, E.B., Melillo, J.M., Kicklighter, D.W., Steudler, P.A., Peterson, B.J., Grace, A.L., Moore, B. III, Vörösmarty, C.J., 1991. Potential net primary productivity in South America: application of a global model. Ecol. Appl. 1, 399–429.

Ramstein, G., Serafini-le Treut, Y., le Treut, H., Forichon, M., Joussaume, S., 1998. Cloud processes associated with past and future climate changes. Climate Dynamics 14, 233–247.

Ritchie, J.C., Cwynar, L.C., Spear, R.W., 1983. Evidence from north–west Canada for an early Holocene Milankovitch thermal maximum. Nature 305, 126–128.

Roeckner, E., Arpe, K., Bengtsson, L., Brinkop, S., Dümenil, L., Esch, M., Kirk, E., Lunkeit, F., Ponater, M., Rockel, B., Sausen, R., Schlese, U., Schubert, S., Windelband, M., 1992. Simulation of the Present-Day Climate with the ECHAM Model: Impact of Model Physics and Resolution. Max-Planck-Institut für Meteorologie, Report 93.

Sadourny, R., Laval, K., 1984. January and July performance of the LMD general circulation model. In: Berger, A., Nicolis, C. (Eds.), New Perspectives in Climates Modelling. pp. 173–198.

Sarmiento, J.L., Toggweiler, 1984. A new model for the role of the oceans in determining atmospheric p_{CO2}. Nature 308, 621–624.

Siegenthaler, U., Wenk, T., 1984. Rapid atmospheric CO_2 variations and ocean circulation. Nature 308, 624–626.

Spero, H.J., Bijma, J., Lea, D.W., Bemis, B.E., 1997. Effect of seawater carbonate concentration on foraminiferal carbon and oxygen isotopes. Nature 390, 497–500.

Street-Perrott, F.A., Perrott, R.A., 1993. Holocene vegetation, lake levels and climate of Africa. In: Wright, H.E.J., Kutzbach, J.E., Webb, T., Ruddiman, W.F., Street-Perrott, F.A., Bartlein, P.J. (Eds.), Global Climates since the Last Glacial Maximum. University of Minnesota Press, Minneapolis, pp. 318–356.

Teeri, J.A., Stowe, L.G., 1976. Climatic patterns and the distribution of C_4 grasses in North America. Oecologia 23, 1–12.

Tinker, P.B., Ineson, P., 1990. Soil organic matter and biology in relation to climate change. In: Scharpenseel, H.W., Schomaker, M., Ayoub, A. (Eds.), Soils on a Warmer Earth, Developments in Soil Science, Vol. 20. Elsevier, Amsterdam, pp. 71–87.

Tushingham, H.M., Peltier, W.R., 1991. A global model of late Pleistocene deglaciation based upon geophysical predictions of post-glacial relative sea level change. J. Geophys. Res. 96, 4497–4523.

van Campo, E., Guiot, J., Peng, C., 1993. A data-based re-appraisal of the terrestrial carbon budget at the last glacial maximum. Global Planet. Change 8, 189–201.

Walker, J.C.G., Opdyke, B.N., 1995. Influence of variable rates of neritic carbonate deposition on atmospheric carbon dioxide and pelagic sediments. Paleoeanography 10, 415–427.

Warnant, P., François, L.M., Strivay, D., Gérard, J.-C., 1994. CARAIB: a global model of terrestrial biological productivity. Global Biogeochemical Cycles 8, 255–270.